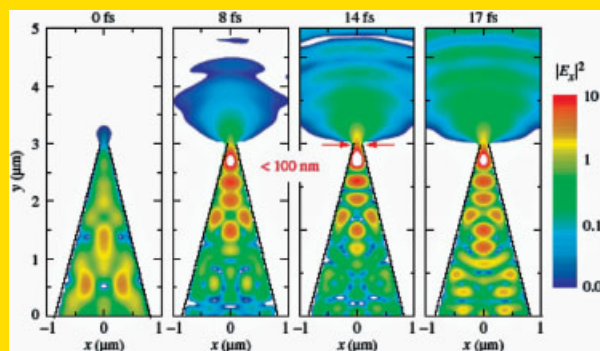


Abstract Ultra-fast nano-optics is a comparatively young and rapidly growing field of research aiming at probing, manipulating and controlling ultrafast optical excitations on nanometer length scales. This ability to control light on nanometric length and femtosecond time scales opens up exciting possibilities for probing dynamic processes in nanostructures in real time and space. This article gives a brief introduction into the emerging research field of ultrafast nano-optics and discusses recent progress made in it. A particular emphasis is laid on the recent experimental work performed in the authors' laboratories. We specifically discuss how ultrafast nano-optical techniques can be used to probe and manipulate coherent optical excitations in individual and dipole-coupled pairs of quantum dots, probe the dynamics of surface plasmon polariton excitations in metallic nanostructures, generate novel nanometer-sized ultrafast light and electron sources and reveal the dipole interaction between excitons and surface plasmon polaritons in hybrid metal-semiconductor nanostructures. Our results indicate that such hybrid nanostructures carry significant potential for realizing novel nano-optical devices such as ultrafast nano-optical switches as well as surface plasmon polariton amplifiers and lasers.



Two-dimensional finite difference time domain (FDTD) simulation of the spatio-temporal evolution of a 10 fs light pulse at a center wavelength of 810 nm propagating through a tapered, perfectly conducting metal-coated fiber probe of 100 nm aperture diameter. The field intensity $|E_x(x, y, t)|^2$ is displayed on a logarithmic intensity scale at four different instants in time. After $t \sim 14$ fs the pulse center reaches the aperture, generating directly below it an ultra-short near-field spot of light.

© 2009 by WILEY-VCH Verlag GmbH & Co. KGaA, Weinheim

Ultra-fast nano-optics

Parinda Vasa^{1,2}, Claus Ropers^{3,4}, Robert Pomraenke¹, and Christoph Lienau^{1,*}

¹ Institut für Physik, Carl von Ossietzky Universität, 26111 Oldenburg, Germany

² Institut für Physik, Technische Universität Ilmenau, 98693 Ilmenau, Germany

³ Courant Research Center Nano-Spectroscopy and X-ray Imaging, University of Göttingen, Friedrich-Hund-Platz 1, 37077 Göttingen, Germany

⁴ Max-Born-Institut, Max-Born-Str. 2A, 12489 Berlin, Germany

Received: 25 October 2008, Revised: 13 January 2009, Accepted: 16 January 2009

Published online: 17 February 2009

Key words: Ultra-fast spectroscopy, near-field microscopy, surface plasmon polaritons, metal and semiconductor nanostructures.

PACS: 68.37.Uv, 73.20.Mf, 82.53.Mj

1. Introduction

A wide variety of elementary physical processes occur on ultrafast, femtosecond time and (sub-)nanometer length scales (Fig. 1). Specific well-known examples are the motion of electronic wave packets in atoms and molecules [1], and the somewhat slower dynamics of vibrational wave packets in molecules [2], typically occurring on Angstrom length and 1–100 fs time scales. Other particularly relevant

processes include, e.g., the (quantum) transport of electronic wave packets in semiconductor nanostructures [3–5], energy transport and electron transfer processes in organic semiconductors [6, 7], and large biomolecules, e.g., the light-harvesting complexes [8]. Most recently, the dynamics of surface plasmon polariton (SPP) excitations in metallic nanostructures, occurring on time scales of 1–100 fs and length scales ranging from a few nm to tens of μm , have attracted increasing attention [9–11].

* Corresponding author: e-mail: christoph.lienau@uni-oldenburg.de

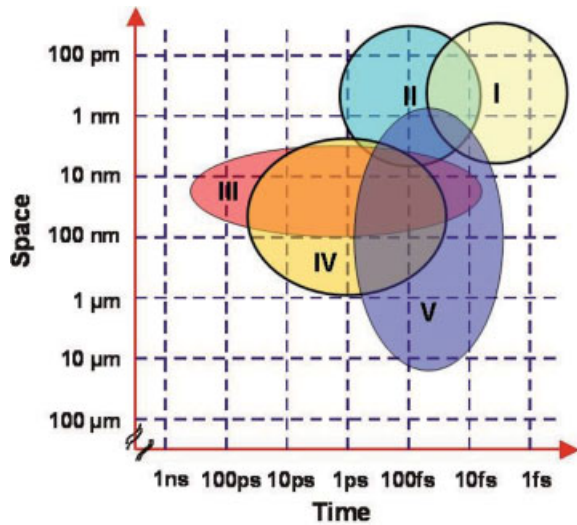


Figure 1 (online color at: www.lpr-journal.org) Examples of elementary physical processes occurring on ultrafast time and nanometer length scales: (I) electronic wave packet propagation in atoms, (II) vibrational wave packet propagation in molecules, (III) electron and energy transport in polymers and large biomolecules, (IV) electronic quantum transport phenomena in semiconductor nanostructures and (V) surface plasmon polariton dynamics in semiconductor nanostructures.

As is immediately apparent from Fig. 1, essentially all of the above-mentioned phenomena involve the motion of optical excitations on subwavelength length scales making a direct space- and time-resolved imaging of these phenomena experimentally challenging. Fig. 2 shows a sketch of

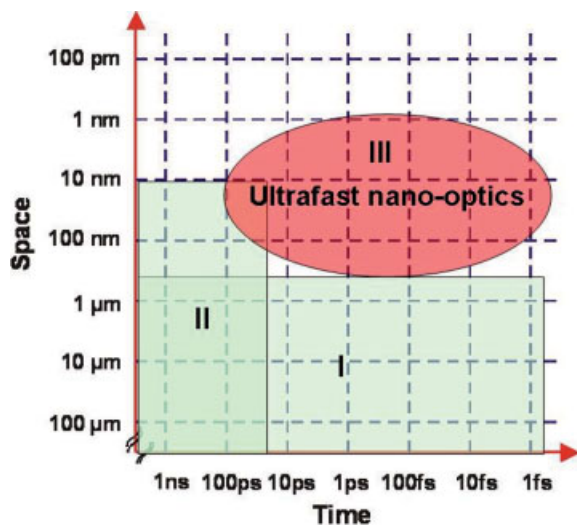


Figure 2 (online color at: www.lpr-journal.org) Experimental techniques for time-resolved optical microscopy: (I) far-field ultrafast optical spectroscopy, (II) time-resolved electron microscopy and cathodoluminescence and (III) ultrafast nano-optics.

the existing time-resolved direct imaging techniques. Ultrafast far-field optical spectroscopy techniques are highly developed, providing time resolution down to the fs range and even below [12]. However, their spatial resolution is inherently diffraction limited by the wavelength of light and rarely goes beyond a few hundreds of nm. Space-time dynamics of electronic and vibrational wave packets in molecules and nanostructures can thus be obtained only indirectly, often requiring additional *a priori* knowledge about potential energy surfaces or the energetics of nanostructures. Electron-based microscopy techniques on the other hand achieve much higher spatial resolution down to the Angstrom range but have generally fairly limited time resolution in the ps domain [13, 14]. Diffraction-based techniques, such as ultrafast electron [15, 16] and X-ray [17–19] diffraction, can provide direct simultaneous space and time resolution. However, they are limited to studies of large ensembles of nanostructures and so far their time resolution reaches only the 100-fs range. This clearly calls for new experimental techniques that can probe the dynamics of optical excitations in *individual* nanostructures on femtosecond time and subwavelength scales.

During the last decade, near-field optical spectroscopy techniques [20, 21], based on evanescent rather than propagating electromagnetic fields, have greatly been improved. Subwavelength optical resolution in the 50-nm and in the 10-nm ranges is now readily reached in numerous laboratories throughout the world using aperture-based [22, 23] and scattering-type ‘apertureless’ [24, 25] near-field probes, respectively. Combining near-field optical spectroscopy and ultrafast laser pulses thus promises the desired simultaneous high spatio-temporal resolution.

It is the aim of this article to give a brief introduction into the current status of the emerging field of ultrafast nano-optics, combining ultrafast and nano-optics in order to probe dynamic processes in *individual* nanostructures in real time and space. Emphasis is laid on briefly reviewing ultrafast optical studies of various classes of nanostructures, ranging from semiconducting and metallic to novel hybrid nanostructures, illustrating the wide application range of these new techniques.

The article is structured as follows. In Sect. 2, a brief introduction into near-field spectroscopy techniques and their combination with ultrafast laser pulses is given [26, 27]. In Sect. 3, we then discuss how ultrafast nanospectroscopy can be used to probe and manipulate coherent optical excitations in single and dipole-coupled semiconductor quantum dots [27–30]. Sect. 4 focuses on ultrafast nano-optical studies of SPP dynamics in metallic nanostructures [11, 31–33]. New concepts for localized ultrafast light and electron sources will also be described [34–38]. Sect. 5 discusses the dipole interaction between excitons and surface plasmon polaritons in hybrid metal-semiconductor nanostructures [39]. Such hybrid nanostructures carry significant potential for realizing novel nano-optical devices such as ultrafast nano-optical switches as well as surface plasmon polariton amplifiers and lasers. Some conclusions and a brief outlook are given in Sect. 6.

2. Experimental techniques

Experimentally, the challenge in combining near-field scanning optical microscopy (NSOM) and ultrafast laser spectroscopy consists in generating ultra-short bursts of light with sufficient temporal and subwavelength spatial resolution. Conceptually, the most straightforward solution to this problem is to funnel ultrafast light pulses through aperture-type near-field fiber probes, as is illustrated in the title figure. The figure shows the results of a two-dimensional finite difference time domain (FDTD) simulation of the spatio-temporal evolution of a 10 fs light pulse at a center wavelength of 810 nm propagating through a tapered, perfectly conducting metal-coated fiber probe of 100 nm aperture diameter [40]. At a time delay $t \sim 14$ fs, the pulse center reaches the aperture, generating directly below it an ultra-short near-field spot of light. Just at the exit, the light spot is spatially localized to the dimension of the aperture diameter. Using clever fabrication techniques, the size of this aperture diameter can currently be reduced to about 30 nm [41]. The simulations indicate a temporal resolution of the evanescent near field directly behind the aperture of about 20 fs, almost a factor of two lower than that of the incident pulses. This decrease in time resolution mainly results from the strongly wavelength-dependent tunneling probability of light through the subwavelength aperture and is a general feature of any aperture probe. In most experiments, however, it turns out that the finite dispersion of the fiber taper, rather than the pulse broadening induced by the aperture, limits the achieved time resolution. In principle, this dispersion can be compensated using higher-order dispersion-compensation schemes. So far, however, in most experiments only second-order dispersion has been balanced and the time resolution in near-field experiments with 50–100 cm long fiber probes was more of the order of 100 fs [26, 42, 43]. These dispersion effects can be avoided by using, e.g., hollow-pyramid near-field aperture probes. Here, time resolution down to 30 fs was shown [44]. As is well known, the drawback of these aperture fiber probes is their low throughput (typically around 10^{-4} – 10^{-5}) along with the low value of the average input power (a few mW) that can be coupled before thermally heating or even damaging the probe [45].

An alternative way of localizing ultrafast laser pulses to spot sizes down to a few nm is to make use of the optical field enhancement at the apex of ultra-sharp metal tapers [46–48]. For a sharp gold taper with a radius of curvature of about 20 nm, as used in Sect. 4.2, and incident pulses polarized along the taper axis, the local field at the apex is enhanced by roughly a factor of 10, resulting in spatially confined nanometer-sized light spots. Such ‘apertureless’ near-field fiber probes are currently used in many exciting applications of ultra-high-resolution optical imaging, ranging from tip-enhanced Raman spectroscopy of single molecules [49] or carbon nanotubes [50] to chemically sensitive infrared spectroscopy [51]. When using such tips for localizing ultrafast light pulses, the achievable time resolution is limited by the finite spectral width of the surface

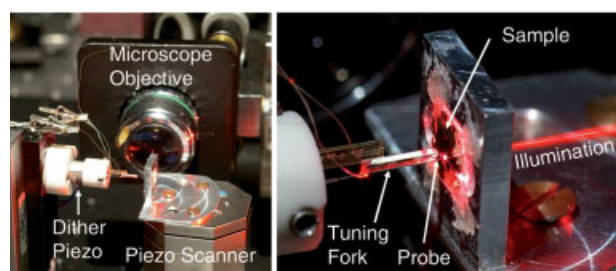


Figure 3 (online color at: www.lpr-journal.org) Photographs of the central part of the near-field microscope. The microscope is based on a hardware-linearized scanner with a scan range of $5 \times 5 \times 5 \mu\text{m}^3$ and employs a horizontal tip orientation.

plasmon resonance in the scattered light spectrum of these tips. These resonances typically lie in the visible to near-IR range and extend over more than 100 nm [52], carrying sufficient bandwidth to support the generation of localized, sub-10-fs pulses. In Sect. 4.2.2, such tips are used for generating spatially localized ultra-short electron pulses. These experiments indeed support the expectation that the time duration of the localized optical field at the apex of such tapers can be reduced to less than 10 femtoseconds [35]. In principle, the performance of such near-field probes can be further enhanced by combining the advantages of both aperture-based and apertureless probe concepts [53, 54]. So far, however, such tip-on-aperture probes have not been combined with ultrafast light sources.

For raster scanning such near-field fiber probes across the nanostructured surface of interest, we use home-built scanning microscopes (Fig. 3) operating either at room temperature or at variable cryogenic temperatures [55], between 10 and 300 K. The instruments are based on a hardware-linearized piezo scanner (Physik Instrumente ‘Picocube’) with a three-dimensional scan range of $5 \times 5 \times 5 \mu\text{m}^3$ and capacitive position detection with a precision of better than 1 nm. The distance between the tip and the sample is regulated by a shear-force feedback system [56], employing a tuning fork sensor [57, 58]. The chemically etched, uncoated [59] or metal-coated fiber tips are glued on a quartz tuning fork mounted on a ‘dither-piezo’. The tuning fork is mechanically excited at its resonant frequency (~ 32.8 kHz) by applying a small AC voltage to the tube dither-piezo. The current induced between the two electrical tuning fork contacts is amplified and detected with a lock-in-amplifier. The experiments are performed with oscillation amplitudes of about 1 nm to achieve high spatial resolution with an amplitude detection noise ratio of less than 5×10^{-3} . In order to avoid mechanical vibrations from the setup, the microscope is placed on a passive vibration-isolated table inside a sound-insulated housing. The experimental setups are versatile and operate with different types of aperture-based and apertureless SNOM probes. They can be used in different experimental configurations in transmission and/or reflection geometry.

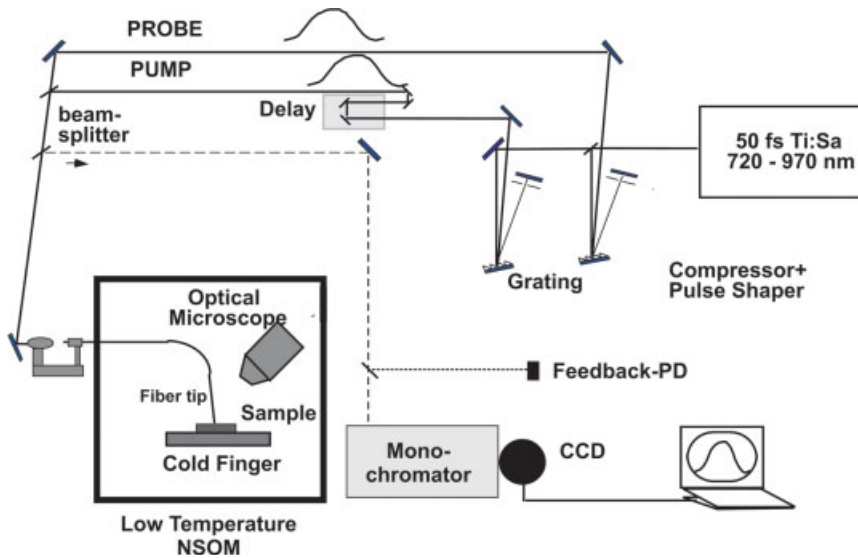


Figure 4 Schematic of the near-field pump-probe spectrometer [26,27]. Pump and probe pulses are derived from a 50 fs, 80 MHz repetition rate Ti:sapphire oscillator. The pulses are spectrally and temporally shaped into two independent compressor units in order to reach less than 200 fs time resolution at the exit of the fiber tip. In the illumination/collection mode, pump and probe pulses are coupled into a near-field fiber probe and the reflected light is collected through the same fiber, spectrally dispersed in a monochromator and detected with a charge-coupled device (CCD) camera. The fiber probe is raster scanned across the sample, which is mounted on the cold finger of a helium flow cryostat [55].

For the low-temperature experiments described in Sect. 3 or the electron experiments described in Sect. 4.2.2, this microscope is installed inside a high-vacuum chamber operating at a base pressure of about 10^{-7} mbar. The chamber is evacuated using a magnetic bearing turbomolecular pump (BOC Edwards), which is kept operating during the course of the experiments.

Depending upon requirements, different continuous-wave (cw) or pulsed laser sources are used in the near-field experiments described here. In the ultrafast experiments, we use either a commercial Ti:sapphire oscillator (Femtolasers ‘Femtosource Rainbow’), emitting 7 fs laser pulses at a center wavelength of 800 nm, or a combination of home-built and commercial (Spectra Physics ‘Tsunami’) spectrally tunable ultrafast lasers delivering pulses with durations between 20 fs and 80 fs. The setup of a typical ultrafast near-field pump-probe spectrometer used in our experiments is illustrated in Fig. 4. Pump and probe pulses are separated by a beam splitter and sent through different grating compressors for spectral shaping and precompensation of group-velocity dispersion experienced in the near-field fiber probes. For the experiments described in the next section, both these pulses are coupled into an uncoated near-field fiber tip. The probe light reflected from the sample is locally collected through the same fiber. The sample is mounted on the cold finger of a helium flow cryostat. For studying the optical nonlinearity of a single semiconductor quantum dot, pump-probe experiments have to be performed at low probe-laser powers of only about 100 nW coupled into the near-field fiber. This requires a pump-probe spectrometer with high detection sensitivity close to the shot-noise limit and combined high spectral resolution. Therefore, the collected light is dispersed in a 0.5 m monochromator yielding a spectral resolution of $60 \mu\text{eV}$ and detected with a high-sensitivity liquid-nitrogen-cooled CCD camera. The signal-to-noise ratio of the CCD detection achieved in this setup is only about a factor of two above the shot-noise limit. Using these uncoated near-

field probes, we reached a spatial resolution of down to 150 nm [60].

3. Probing the optical nonlinearity of a single semiconductor quantum dot

In semiconductor quantum dots (QDs), electron and hole wave functions are localized in all three spatial dimensions on a nanometer length scale due to growth-induced nanoscale variations of the semiconductor composition. As has been proven in numerous experiments over the last few years, the linear optical properties of semiconductor quantum dots are surprisingly similar to those of atomic systems. They reflect an atomic-like density of states [61–63], a shell-like energy structure [64] and rather long dephasing times of excitonic and spin excitations on the ns scale [65, 66]. This makes excitonic and spin excitations of QDs interesting candidates for solid-state-based implementation of quantum logic. Such implementation requires a precise manipulation and readout of these excitations with a time resolution which is much faster than their dephasing times. This clearly calls for ultrafast studies of the nonlinear optical properties of individual QDs.

Why did we decide to use ultrafast near-field spectroscopy to study their nonlinear optical properties? Firstly, we wanted to study specific QD model systems, so-called ‘interface’ QDs resulting from local thickness fluctuations in thin gallium arsenide quantum wells (Fig. 5a and b). These QDs are attractive because at the time when we started our experiments (i) their linear optical properties were particularly well understood and (ii) these samples are particularly clean, showing little unwanted effects such as spectral fluctuations due to charge fluctuations in the QD environment. In these samples, the statistical distribution of the lateral quantum well (QW) thickness fluctuations gives rise to a pronounced inhomogeneous broadening of far-field optical spectra. In experiments with sufficiently

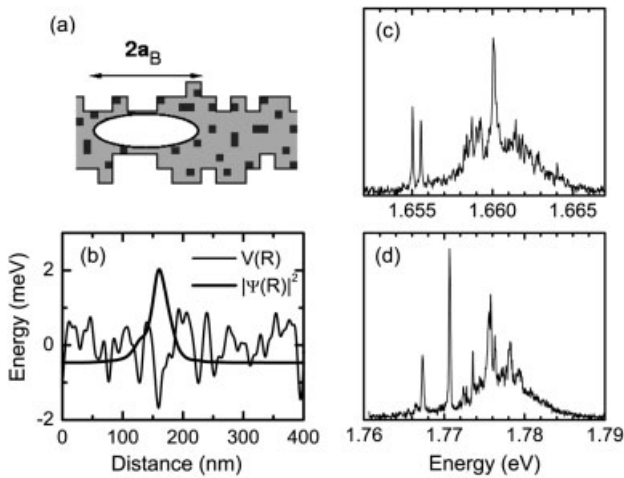


Figure 5 Localized excitons in a thin QW [27]. (a) Disorder in QWs arises from spatial fluctuations of the local QW thickness (interface roughness) and of the QW composition (alloy disorder). (b) Schematic of the effective disorder potential $V(R)$ and of a localized excitonic center-of-mass wave function $|\Psi(R)|^2$. Representative near-field PL spectra at 12 K of (c) a 5.1 nm thick and (d) a 3.3 nm thick (100) GaAs QW.

high spatial and spectral resolution, however, the smooth inhomogeneously broadened photoluminescence (PL) spectra break up into narrow emission lines from a few localized excitons as seen in Fig. 5c and d. At low temperatures, the narrow excitonic lines display rather long dephasing times of 20–50 ps, a prerequisite for implementation of quantum logical operations. High spatial resolution is thus essential for isolating individual QDs. In these experiments, we therefore used a near-field fiber probe to spatially localize and isolate a selected QD with a particularly interesting PL spectrum. We then positioned the near-field probe at this dot and continued probing its nonlinear optical properties. Since the nonlinear measurements require a rather long measurement time of up to one hour, it evidently requires a rather stable low temperature microscope setup. During the course of the nonlinear measurements, we constantly monitored the PL spectrum to ensure accurate positioning of the near-field probe with respect to the QD of interest.

Performing these experiments in a high-spatial-resolution near-field spectrometer has an additional important advantage over far-field detection schemes. It greatly increases the nonlinear optical signal which can be retrieved from a single QD. To first order of approximation, the nonlinear optical signal is proportional to the square of the ratio between the QD absorption cross section σ and the optical resolution A_0 , $(\sigma/A_0)^2$. A factor of 10 improvement in optical resolution thus enhances the nonlinear optical signal by two orders of magnitude. This is nicely illustrated in Fig. 6, comparing the differential reflectivity ΔR and PL spectra recorded under identical excitation conditions for single-exciton transitions in five different QWs buried at distances from 95 to 211 nm below the

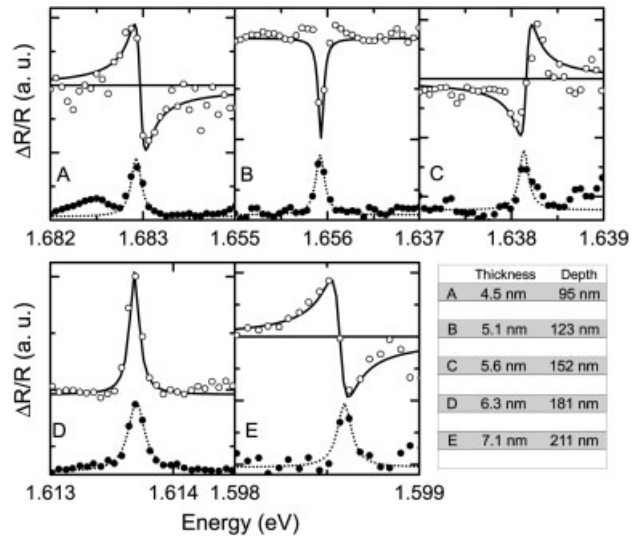


Figure 6 Differential reflectivity spectra (open circles) of five interface QDs located at different depths of 95 to 210 nm below the sample surface (see inset) [27, 28]. The differential reflectivity spectra are recorded by using a non-resonant pump pulse with 100 fs time duration to create electron-hole pairs in 2D continuum states and probing the induced change in reflectivity of a time-delayed probe pulse. The time delay is set at 10 ps. The differential reflectivity spectra are compared with simultaneously recorded PL spectra (solid circles). Note the transition between dispersive and absorptive line shapes.

surface. Firstly, the experiments show that for all excitonic resonances resolved in the PL spectra, a corresponding resonance occurs in the nonlinear optical spectra at precisely the same energy. This is a clear indication that individual QDs are indeed probed. Second, the maximum amplitude of the nonlinear signal, recorded in a reflection geometry, amounts to more than 1%. Such a high signal is a clear signature for the high spatial resolution achieved in these experiments. A very interesting feature in these experiments is the drastic change in line shape of the nonlinear spectra when varying the distance between QW and surface. The spectra show a clear transition between dispersive (A, C and E) and absorptive line shapes (B and D). This transition can be understood by analyzing the origin of these reflectivity spectra in more detail [27, 28]. In these experiments, a fraction of the spectrally broadband incident probe laser light is back reflected from the surface of the semiconductor into the near-field fiber probe. Another part of the probe laser light propagates into the semiconductor crystal and resonantly excites QD excitons. These excitons re-emit dipole radiation and a part of this radiation is also coupled back into the fiber probe. The reflectivity spectrum is then given as the spectral interferogram between the probe laser light reflected from the sample surface and the electromagnetic field locally emitted by the QD. The differential reflectivity spectra monitor the pump-induced changes in this spectral interferogram resulting from the

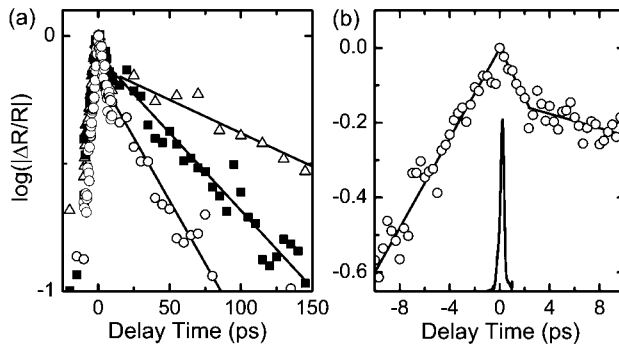


Figure 7 Temporal dynamics of $\Delta R/R_0$ for three different QD resonances at 1.6598 eV (circles), 1.6614 eV (triangles) and 1.6648 eV (squares). In these experiments [28], the off-resonant pump laser creates electron-hole pairs in QW continuum states. The dynamics are displayed on a logarithmic ordinate scale. All decays are bi-exponential with a slow decay time varying between 30 and 150 ps. (b) Early time $\Delta R/R_0$ dynamics of a single QD resonance. A slow rise of $\Delta R/R_0$ is observed at negative time delays. The time resolution of the experiment is 150 fs, as indicated by the cross-correlation measurement (solid line around $\Delta t = 0$).

pump-laser-induced modification of the emitted QD field. This interferogram evidently depends on the relative phase of both the reflected probe and the QD field. This relative phase now increases roughly as $2 \times n_s \times d$, with n_s being the refractive index of the semiconductor, when increasing the spatial separation d between QD and surface. At a depth of 123 nm (QD B), the probe laser field and the pump-induced change in QD field are almost exactly 180° out of phase, giving rise to an ‘absorptive’ line shape in ΔR . Increasing the depth by 29 nm (QD C) increases the phase difference by $\simeq 90^\circ$, resulting in a ‘dispersive’ line shape. The distance dependence of the spectra can thus be quantitatively understood within such a simplified local oscillator model. Similar interference effects are also observed in the linear spectra of periodic metal nanostructures and will be discussed in Sect. 4.1.

We now briefly discuss the time dependence of the optical nonlinearity of a single interface QD [28]. Transient differential reflectivity ($\Delta R/R_0$) measurements as a function of time delay between the pump and probe pulses are shown in Fig. 7. In these measurements the off-resonant pump pulses at 1.675 eV (power 120 nW) create about five electron-hole pairs per pulse in QW continuum states. These electron-hole pairs can quickly relax into the QDs on a 2 ps time scale (the fast decay at positive time delays in Fig. 7b). This carrier trapping into the QD results in a bleaching of the QD absorption, which vanishes on a 50 ps scale due to the rapid radiative recombination of the electron-hole pairs in the QD. The measurement therefore provides a direct measure of the exciton lifetime and thus the QD dipole moment. Estimated values of the dipole moment d_{QD} for the observed decay times between 150 and 50 ps are 50–85 D. The values exceed those observed

in atomic systems by more than an order of magnitude and reflect the large spatial extension of the exciton center-of-mass wave function in these QDs of several tens of nanometers (Fig. 5a and b). A striking feature of these measurements is the strong nonlinear signal at *negative* time delays, i.e., when the probe laser precedes the pump laser. A detailed analysis [28] shows that this signal reflects the so-called perturbed free induction decay of the quantum dot polarization. The resonant probe laser creates a coherent superposition of the QD electron states in the valence and conduction bands. It thus induces a coherent polarization which persists, in the absence of a pump laser, for at least 30 ps due to the long QD dephasing time. The pump laser now excites electron-hole pairs in QW continuum states creating a fluctuating charge environment of the QD. These charge fluctuations can destroy the coherent QD polarization, resulting in the strong nonlinear optical signal at negative time delays. The observed perturbed free induction decay is a clear signature that, in contrast to atomic systems, many-body interactions can have a strong effect on QD optical nonlinearities. Resonant excitation schemes are needed to suppress such many-body interactions.

A hallmark of the coherent interaction between a generic two-level system and a resonant pulsed laser field are Rabi oscillations in the excited-state population. Observing Rabi oscillation in semiconductor QDs therefore was a crucial step in exploring the analogy between QD and atomic systems [67, 68]. Such Rabi oscillations (Fig. 8) can also be probed with the ultrafast near-field spectrometer described in the previous section [30]. The QD exciton should be resonantly and impulsively excited with light pulses much shorter in duration than the exciton dephasing time. In our experiments, this was achieved by tuning spectrally tailored optical pulses with a spectral width of ~ 1 meV and a pulse duration of ~ 1.5 ps in resonance with the exci-

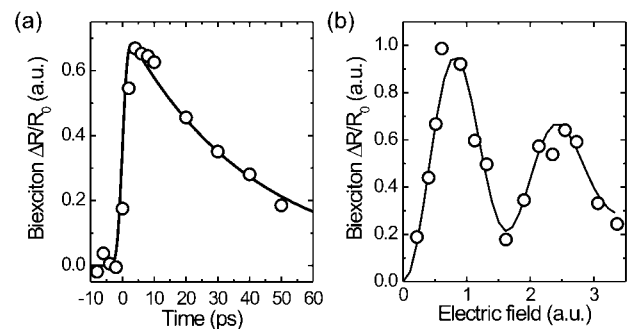


Figure 8 Demonstration of Rabi oscillations in a single QD [30]. (a) A pump laser is tuned in resonance with the excitonic transition of a single QD. A weak, time-delayed probe laser, resonant with the exciton-to-bi-exciton transition of the QD, monitors the exciton population. The time dependence of the differential probe reflectivity $\Delta R/R_0(t)$ therefore monitors the time decay of the QD exciton population dynamics. (b) Differential probe reflectivity at a fixed time delay $\Delta R/R_0(t = 10 \text{ ps})$ as a function of the maximum electric field strength of the pump laser.

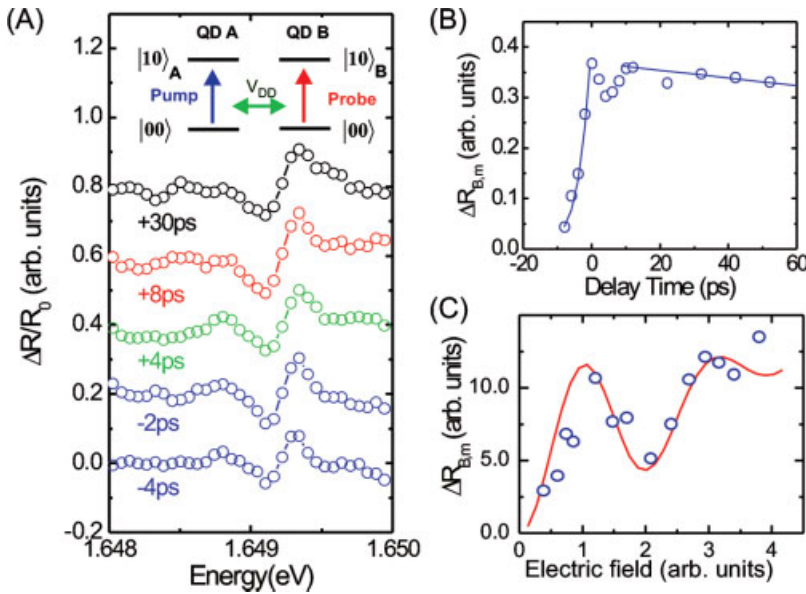


Figure 9 (online color at: www.lpr-journal.org) (a) Demonstration of Rabi oscillations in two dipole-coupled QDs [30]. In these experiments, the excitonic resonance of the same QD (QD A) as in Fig. 8 is resonantly excited by the pump laser. The differential reflectivity spectrum ($\Delta R/R_0$) is now probed in the spectral window around the excitonic resonance of a neighboring QD (QD B). The $\Delta R/R_0$ spectrum of QD B shows a dispersive line shape at all delay times, indicating a transient shift of the resonance due to dipole-dipole interactions. (b) Amplitude of $\Delta R/R_0$ of QD B as a function of time delay between pump and probe pulses. (c) Amplitude of $\Delta R/R_0$ of QD B at a fixed time delay of 10 ps as a function of the maximum electric field strength of the pump laser. The observed Rabi oscillations prove that a manipulation of the exciton population of QD A affects the nonlinear optical response of QD B.

tonic transition of a specifically selected QD. Furthermore, a read out of the transient exciton population is needed. We performed this read out by probing the time-dependent differential reflectivity $\Delta R/R_0$ at the exciton-to-bi-exciton transition of the selected QD. Due to the strong Coulomb interaction between excitons in QDs this transition is red shifted by about 3 meV from the QD exciton transition. The time dependence of this differential reflectivity is shown in Fig. 8a. It clearly monitors the decay of the exciton population on a 30 ps time scale due to the rapid radiative QD recombination. Rabi oscillations can be observed when monitoring the differential reflectivity at a fixed time delay between pump and probe $\Delta R/R_0$ ($t = 10$ ps) in dependence on the intensity of the pump laser, see Fig. 8a. The maximum nonlinearity corresponds to an exciton density close to unity, i.e., to an almost complete inversion of the QD two-level-system. Further increase in pulse intensity decreases the nonlinearity due to the onset of stimulated emission. Despite the clarity of these oscillations, the results also show that these QDs are not an ideally isolated two-level system. The bi-excitonic nonlinearity corresponding to the second maximum is $\sim 1/3$ smaller than the first maximum indicating presence of additional decoherence sources. Such a reduction in the fidelity of Rabi oscillations at high fields has now been observed in various QD systems. Despite the recent progress in understanding the underlying physical mechanism, it is not yet fully established how to suppress these unwanted decoherence phenomena.

The above-mentioned measurements have been performed with spectrally broad probe-laser pulses with a width of about 10 meV. With our CCD-based detection we can probe the nonlinear optical response of all excitonic transitions that fall within the spectral window of the probe laser. Since the spatial resolution in these experiments was about 250 nm, we generally probed reflected light from several different localized excitons simultaneously. This

allowed us to go beyond probing the nonlinear response of an individual QD and to investigate how the coherent manipulation of one QD affects the optical nonlinearity of an adjacent QD. First experimental results probing the nonlinear optical response of laterally coupled QDs are displayed in Fig. 9. In these experiments, the excitonic resonance of the same QD (QD A) as in Fig. 8 is resonantly excited by the resonant pump laser. Now, we probe the differential reflectivity spectrum ($\Delta R/R_0$) in the spectral window around the excitonic resonance of a *neighboring* QD (QD B). The ($\Delta R/R_0$) spectrum of QD B shows a dispersive line shape at all delay times. This dispersive line shape indicates a transient blue shift of the excitonic resonance due to dipole-dipole interactions between both QDs. From the amplitude and shape of the nonlinear spectra, we deduce a line shift of 30 ± 15 μ eV around zero time delay. The time evolution of the maximum amplitude of $\Delta R/R_0$ of QD B is very different from that observed at the bi-exciton resonance of QD A (Fig. 8a). It shows a rise with a time constant of about 6 ps at negative time delays, followed by a slower decay on a 100 ps time scale. When we plot the amplitude of $\Delta R/R_0$ of QD B at a fixed time delay of 10 ps as a function of the maximum electric field strength, we observe again pronounced Rabi oscillations (Fig. 9c). These oscillations prove that a manipulation of the exciton population of QD A directly affects the nonlinear optical response of QD B, thus demonstrating transient dipole-dipole interactions between both QDs.

It is *a priori* not clear what the microscopic mechanism underlying these dipolar interactions is. In atomic systems, Förster coupling between optically induced oscillating transition dipole moments dominates [69, 70]. Detailed theoretical analyses [30, 71] show, however, that Förster couplings would give rise to absorptive line shapes in the nonlinear spectra, which are not observed. Therefore, we conclude that the Förster coupling between the probed QDs is too

weak to be detected. Our results indicate that the optical excitation of QD A apparently results in transient dipole moments (resulting from a spatial separation of the centers of mass of the electron and hole wave functions in the QD [72, 73]) in the two dots [30]. Our experiments probe the direct dipole coupling between these induced dipole moments. Detailed theoretical modeling shows that both the observed Rabi oscillations and the line shape of the nonlinear spectra are consistent with this conclusion.

The observed coupling strength of $30 \mu\text{eV}$ is in good agreement with theoretical estimates if we assume that the two quantum dots are separated by about 15–20 nm. However, so far, in our experiments this distance could not be measured independently.

It would be very interesting to use such dipole-coupled quantum dots for implementing various two-qubit quantum logic operations, as already proposed several years ago [72]. So far, however, the measured interaction strength is about one order of magnitude too small for quantum gate operations. The recent success in controlling the coupling strength in quantum dot molecules by means of moderate electric fields [74] promises progress in this direction. We also wish to point out that the powerful experimental tools for probing optical nonlinearities with subwavelength spatial resolution described in this section will certainly be of interest for exploring the nonlinear optics of novel metal-semiconductor hybrid nanostructures discussed in Sect. 5.

4. Ultra-fast surface plasmon polariton nano-optics

Plasmonics forms a major part of the fascinating and emerging field of ultrafast nano-optics. It is based on the unique optical properties of metals arising from the interaction of a large density of mobile conduction electrons with electromagnetic radiation [75]. The optical dispersion in metals can be described by a complex dielectric function $\epsilon_m(\omega)$ having a large negative real component which gives rise to high reflectivity over a broad spectrum spanning from the far infrared to the ultraviolet and forms the basis for the topics discussed in this section.

Due to the large number of mobile electrons, light impinging on a metal surface induces charge and current oscillations known as surface plasmons within the skin depth of the metal surface. Oscillating charges in turn create an optical field near the surface that modifies the surrounding field acting on them. This mutual interaction results in the combined resonant modes of the electron motion with a surface-bound electromagnetic field, which are known as surface plasmon polaritons (SPPs). For a planar metal-dielectric interface, the dispersion relation of these evanescent SPPs is given by $k_{\text{spp}} = \frac{\omega_{\text{spp}}}{c} \sqrt{\frac{\epsilon_m \epsilon_d}{\epsilon_m + \epsilon_d}}$, where k_{spp} is the complex SPP wave vector, ω_{spp} is its angular frequency and ϵ_d is the dielectric constant of the surrounding medium with $\text{Re}(\epsilon_d > 0)$ [75]. As the SPP momentum is larger than that of the incoming photon, excitation of SPPs

requires special configurations which allow momentum conservation like in total internal reflection by a metal-coated prism (Kretschmann configuration) or scattering by metal gratings and other nanostructures [11, 32, 75]. Due to the large momentum vector, the SPP wavelength can be much smaller than the photon wavelength and therefore SPP-based microscopy can offer much higher spatial resolution than conventional optical microscopy even at visible photon energies. Due to the small electron scattering time scales in metals, the SPPs are highly damped resonances with exceedingly short lifetimes, typically in the range of femtoseconds. Though the propagation lengths of SPPs on a smooth continuous metal surface can be as large as several millimeters [76] for near-infrared wavelengths, due to the reduced resistive losses in metals in this wavelength range, any discontinuity of the metal surface on the scale of the wavelength significantly decreases their propagation length. Enhanced damping on nanometric metal structures mainly arises from the scattering of the SPPs into the far-field radiation [32]. Therefore, the SPPs exhibit very different characteristics depending on the sample geometry showing extremely strong localization effects when excited on highly curved geometries, e.g., on metal nanoparticles or on sharp metal tapers (NSOM probes), leading to localized fields which may far exceed those incident on the surface. Much shorter wavelengths at visible photon energies coupled with high field localization, fast response times and the possibility of altering the characteristics by merely changing the structural parameters make SPPs ideal for several applications in opto-electronics, biology and medicine with spectroscopic applications being on the forefront. SPPs are already being widely used to enhance Raman scattering [77], molecular fluorescence [78] and the output efficiency of solid-state light emitters [79] and terahertz lasers [80]. Commercial SPP-based ellipsometers [81] are capable of tracing minute amounts of substance, e.g., in the detection of protein monolayers or to monitor antibody reactions [82]. Field localization properties of SPPs have also recently been used to demonstrate trapping of micro-colloids on a patterned metal surface under low laser intensity. Force microscopy reveals that such plasmon traps provide stable trapping with forces in the range of a few tens of femtonewtons at extremely low laser intensities compared to those produced by light [83].

At present an exciting theme in plasmonics that is expected to make SPPs even more relevant in ultrafast nano-optics is the control of SPP propagation and localization on the nanoscale [10, 84]. A prominent early example was the achievement of a very high optical transmissivity through periodic arrays of very small subwavelength apertures in thin metal sheets. Periodically patterned metal structures known as ‘plasmonic crystals’ are ideal model systems for tailoring and investigating SPP properties by merging the well-understood concepts of photonic crystals [85] with the exceptional properties of metals. The SPPs excited in such plasmonic crystals are strongly coupled to optical far fields, which limits their lifetimes to a few tens of femtoseconds and propagation lengths to a few microns [32, 86]. There-

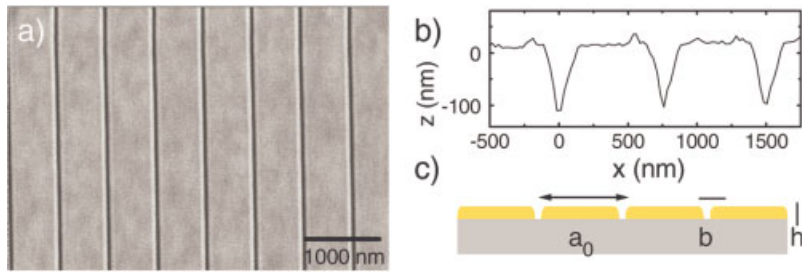


Figure 10 (online color at: www.lpr-journal.org) Periodically patterned thin-film gratings [11, 32, 33]. (a) Scanning electron micrograph of a one-dimensional slit array in a gold film. (b) Cross section as measured by scanning shear-force microscopy. (c) Definitions of the structural parameters: lattice period a_0 , slit width d and film thickness h .

fore, to be able to efficiently use them in applications, it is necessary to have a better understanding of the ways to control SPP damping. Due to the short SPP lifetime and propagation length as well as the small scale of the structures involved, investigation of SPP dynamics or SPP-based nano-optics often requires experimental techniques which can give a temporal resolution of a few femtoseconds and nanometric spatial resolution.

In this section, we discuss some of the recent experimental work in probing and understanding the elementary properties of SPPs and developing SPP-based microscopes to achieve high spatio-temporal resolution. The section is divided into three parts. The first part deals with our experiments aimed at investigating the SPPs excited on one-dimensional plasmonic crystals by combining ultrafast laser spectroscopy and nano-optical imaging techniques [11, 32, 33]. The second part is about the recent development of two SPP-based nanosources for scanning microscopy recently reported by our group. One of them is generated by launching SPPs on metal nanotips [34]. This novel probe is expected to enhance the capabilities of apertureless SNOM by reducing the background signal while maintaining high spatial resolution. The other is a nanoscopic single-electron source which can give femtosecond temporal and nanometric spatial resolution in electron-emission microscopy [35, 36]. In the last subsection, we discuss techniques recently proposed by Aeschlimann *et al.* and Stockman *et al.* for controlling and localizing the nano-optical SPP fields so that high spatio-temporal resolution can be achieved in conventional far-field spectroscopy or photoelectron microscopy [37, 38].

4.1. Light localization and SPP excitations in metallic nano-arrays

It is the aim of this section to demonstrate that the combination of coherent optical techniques and spatially resolved spectroscopic techniques discussed earlier in Sect. 2 yields a clear picture of the microscopic physical phenomena governing the linear optical properties of metallic arrays. Specifically, we want to show that such experiments provide detailed insight into the – partially very controversially discussed [87, 88] – role that SPPs play in enhancing the transmission through periodic arrays of small holes or slits in metal films [9]. In these studies, we also find new and ini-

tially unexpected phenomena such as the strong subradiant suppression of SPP damping in nanoslit arrays [11].

A typical one-dimensional metal slit array discussed here is shown in Fig. 10. The sample consists of a $h = 150$ nm thick gold film perforated by linear arrays of $d = 50$ nm wide nanoslits with periods of $a_0 = 650$ and 750 nm. The grating parameters are chosen to match the wavelength range of interest, i.e., that of a broadband, 7 fs Ti:sapphire laser. The samples are fabricated either by electron-beam lithography or by focused ion-beam milling on a flat sapphire substrate [11, 32].

In the conventional angle-resolved linear transmission experiments presented here, the nanoslit array is illuminated with p-polarized light from a broadband Ti:sapphire laser, with its electric field vector perpendicular to the slit axis. In this case, SPPs are excited at both air-metal (AM) and sapphire-metal or semiconductor-metal (SM) interfaces by transferring momentum $n \frac{2\pi}{a_0}$, $n \in \mathbb{Z}$, to the incident photons [11, 32, 75, 89]. Angle-dependent transmission spectra of such nanoslit arrays shown in Fig. 11 reveal the pronounced enhancement of the transmission at certain resonance wavelengths corresponding to the excitation of different AM and SM resonances.

Based on such angle-resolved transmission and reflection spectra, the dispersion relation of these resonances, particularly their asymmetric line shapes compared to those symmetric line shapes observed in Kretschmann configurations, have been debated [9, 90]. Here, we show that the coherent optical experiments discussed here can give important additional information that may help in clarifying some of these issues. In this work, spectral interferometry [91] is used to measure both amplitude and phase of the angle-dependent linear transmissivity $\text{tr}(\omega)$. In this technique, the transmitted pulse from the metal grating is interfered with a reference pulse from the laser with known amplitude and phase spectrum (measured by spectral phase interferometry for direct electric-field reconstruction, SPIDER) [92, 93]. The spectral intensity of the generated interference pattern is used to characterize the transmitted electric field [11, 33]. The relation between electric field amplitudes of the incident and transmitted pulses is given by the equation

$$E_{\text{out}}(\omega) = \text{tr}(\omega) E_{\text{in}}(\omega), \quad (1)$$

and the transmission spectrum is $\text{Tr}(\omega) = |\text{tr}(\omega)|^2$. Detailed insight into the physical origin of these complex spectral variations can be obtained by plotting the spectral

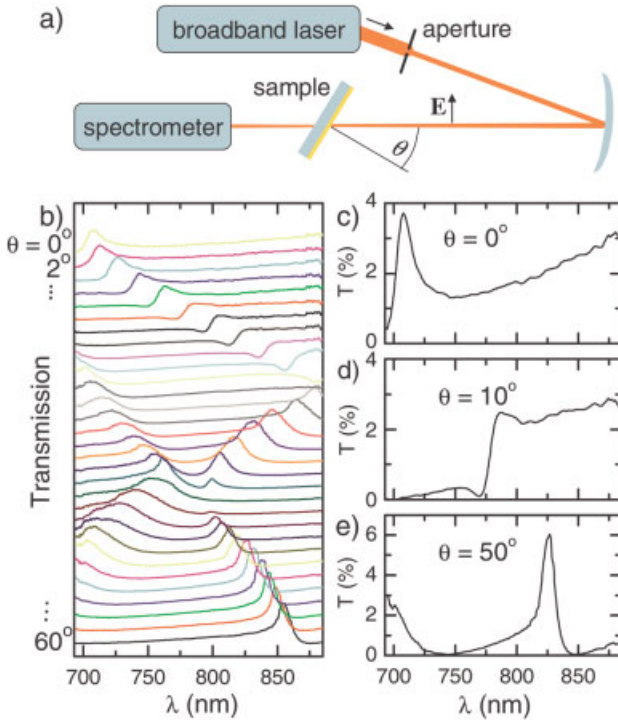


Figure 11 (online color at: www.lpr-journal.org) Angle-dependent transmission spectra of a gold nanoslit grating with $a_0 = 650$ nm, $d = 50$ nm and $h = 150$ nm on a sapphire substrate [33]. (a) Experimental setup. The incident p-polarized laser light is sent through an aperture and weakly focused onto the sample with a spherical mirror ($f = 30$ cm). (b) Transmission spectra in steps of $\theta = 2^\circ$. (c)–(e) Three examples of transmission spectra for the indicated angles.

intensity (Fig. 12a) and the time structure of the field $E(t)$ (Fig. 12b) of the pulse transmitted at an angle of 8° through the 650 nm slit array. Fig. 12c shows the time-gated transmission spectrum, obtained by convoluting $E(t)$ with a time-shifted Gaussian window function of 20-fs width and by Fourier transforming the convoluted field function [33] of the transmitted field.

This image shows quite clearly that the light spectrum transmitted through the nanoslit array undergoes a pronounced temporal evolution. Initially it consists of an ultra-fast burst of light covering essentially the entire spectrum of the incident laser. This corresponds to a non-resonant ‘direct’ transmission of the incident light through the nanoslits, without excitation of SPPs at the grating interfaces [90, 94]. At later times, a rather long-lived emission from SPP excitations – in this example from the AM[−1] SPP excitation at around 390 THz (770 nm) – is observed [11]. In the spectral domain, the interference between these two transmission channels gives rise to characteristic asymmetric line shapes [90]. Such an asymmetric (Fano) line shape is generally observed whenever a continuum is coupled to a resonance, for instance in the auto-ionization process in atomic physics [95, 96]. Within a phenomenological model,

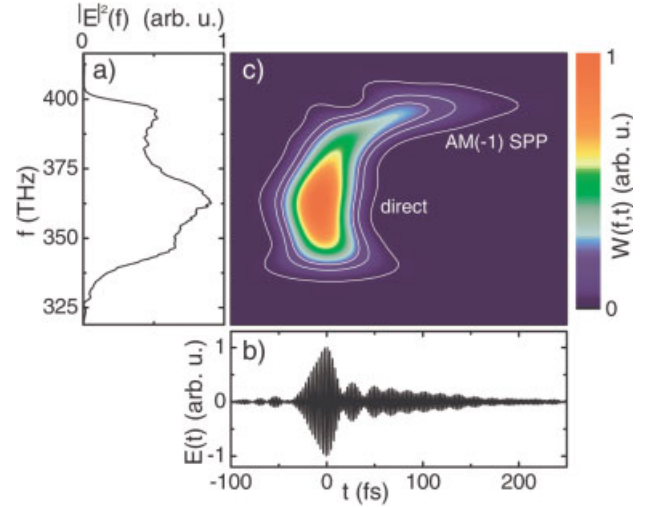


Figure 12 (online color at: www.lpr-journal.org) (a) Optical spectrum of the pulses transmitted through a 650 nm slit array at an angle of $\theta = 8^\circ$. (b) Pulse structure in the time domain. (c) Time-gated transmission spectrum obtained by convolution with a time-shifted 20-fs window function showing that the transmitted pulse consists of an initial burst and a delayed long-lived SPP contribution [33].

the complex transmissivity can be written as

$$\text{tr}(\omega) = a_{\text{nr}} + \sum_j \frac{a_j e^{i\phi_j} \Gamma_{\text{rad},j}}{\omega - \omega_j + i(\Gamma_{\text{rad},j} + \gamma_j)}. \quad (2)$$

Here, a_{nr} is the spectrally flat or slowly varying non-resonant transmission amplitude, and a_j and ϕ_j are the oscillator strengths and phases, respectively. The frequencies ω_j correspond to SPP resonances at either the AM or SM interface. The resonance widths Γ_j contain two terms: a non-radiative damping γ_j due to absorption in the metal, and the radiative damping $\Gamma_{\text{rad},j}$ of the SPP modes, which is dominant for nanoscopic metal structures.

Fig. 13 illustrates the physical picture underlying this line-shape model and shows that the spectral dependences of both $\text{Tr}(\omega)$ and $\varphi(\omega)$ are satisfactorily reproduced. The model also shows that, as illustrated in Fig. 13b, the resonant excitation of SPPs gives rise to an enhancement of the transmission at certain wavelengths due to the coherent superposition of resonant and non-resonant transmission channels [9]. In the samples we have investigated so far, we find, both for slit and hole nano-arrays, a maximum enhancement of the transmission due to resonant SPP excitation by a factor of about 10. Fig. 13c also nicely shows that SPP excitation can have a detrimental effect on the transmission [88]. On the red side of the transmission resonance, the fields emitted directly and via resonant SPP excitation are 180° out of phase and hence destructive interference can completely suppress the transmission at certain wavelengths (around 820 nm in Fig. 13c).

This simple line-shape model now forms a sound basis for a quantitative analysis of the coherent SPP cou-

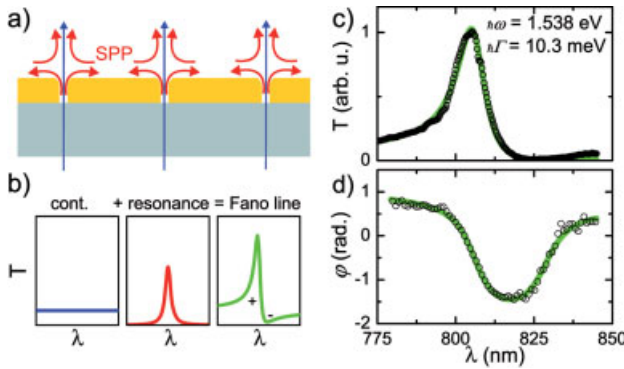


Figure 13 (online color at: www.lpr-journal.org) (a) Physical picture underlying the enhanced transmission through the nanoslit array arising from interference of ‘resonant’ (red) and ‘direct’ (blue) transmission components. (b) Illustration of a Fano-type resonance as the interference between a broadband continuum component (direct transmission) and a resonant (SPP) contribution, resulting in constructive (+) and destructive (–) interference of both components in the far field. (c,d) Simultaneous fit of a Fano resonance (green lines) to the squared magnitude (c) and the spectral phase (d) of the measured complex transmissivity (open circles) at $\theta = 44^\circ$ [11, 33].

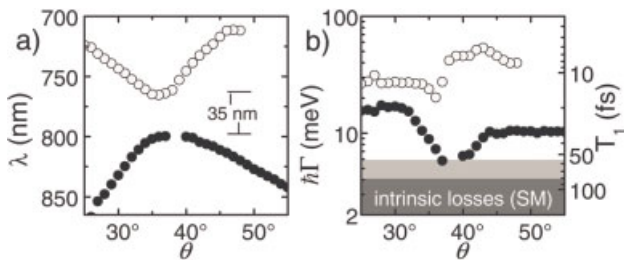


Figure 14 Formation of a plasmonic band gap for substrate-metal SPPs, evaluated from a fit to the Fano line shape [11, 33]. (a) Resonance wavelengths of the upper and lower SPP branches. (b) Line widths and corresponding lifetimes of both branches (logarithmic scale). The upper borders of the light gray and gray shaded areas correspond to the expected intrinsic (absorptive) SPP damping for the dielectric function of a planar dielectric/metal interface.

pling between different SPP resonances, namely the formation of band gaps in the transmission spectra of such nanoslit or hole arrays [11]. In Sect. 5 we will show that a similar model can be used to explain the interaction between SPPs and excitons in QWs [39]. Coherent interactions are expected to become important whenever two or more SPP modes are brought into resonance. These interactions arise from the scattering between both SPPs induced by the nanoslit grating. The essential consequences of such interactions are summarized in Fig. 14 for the crossing of the SM[+1] and SM[–2] modes of the nanoslit array with $a_0 = 650$ nm. To obtain these data, we have numerically analyzed linear angle-resolved far-field transmission spectra (Fig. 11) using the line-shape model de-

scribed above (Eq. 2). The extracted resonance wavelengths $\lambda_j = 2\pi c/\omega_j$, widths Γ_j and SPP lifetimes $T_{1,j} = 1/(2\Gamma_j)$ are shown in Fig. 14a and b, respectively. A clear anti-crossing of the two SPP branches near $\theta = 38^\circ$ and the formation of a plasmonic band gap with an energy 72 meV are observed. Even larger band gaps can be observed when coupling localized SPP modes to external waveguide modes [97].

In addition to the splitting of the resonance frequencies, drastic intensity and line-width variations are found close to the crossing. The line widths of the upper and lower branches are plotted in Fig. 14b as the open and black circles, respectively. The most striking feature is the line-width narrowing of the lower-energy branch near to $\Gamma \approx 5.5$ meV corresponding to a SPP lifetime of about 60 fs, which is much closer to the non-radiative damping time than the lifetimes of the SPP resonances of a few fs. The apparent asymmetry of the damping constants about the crossing angle (Fig. 14b) arises because of the coupling of different SPP modes. Near the anti-crossing, the SPP lifetime is no longer limited by radiative damping but by the intrinsic SPP losses. In addition, the intensity of the transmission decreases and eventually vanishes near the anti-crossing angle $\theta = 38^\circ$. This line narrowing is evidence for a coupling-induced suppression of radiative damping or subradiance, which is further confirmed by spectrally resolved near-field imaging of the optical modes in these plasmonic crystals (Fig. 15).

Near-field imaging of SPP fields reveals the physical origin of this damping suppression. Here, the sample is illuminated through the sapphire substrate near $\theta = 0^\circ$ using the broadband Ti:sapphire laser. The transmitted light is scattered off an Al-coated near-fiber probe, dispersed in the far field through a monochromator and detected with a CCD camera. These experiments are performed on a grating with a period $a_0 = 750$ nm, in the spectral region around the crossing of the AM[+1] and AM[–1] SPP modes [11, 98]. Fig. 15b shows the spatially averaged near-field spectrum, normalized to the incident spectrum. The broad and the narrow resonances found in the far-field transmission forming the air-metal SPP band gap are evident. Most important are the spatial near-field intensity distributions $I(x)$ along the surface at the wavelengths of the narrow (*dark*) and broad (*bright*) resonances (Fig. 15b). In the wavelength range of the broad resonance, $I(x)$ shows maxima at the slits and slightly weaker maxima in the center between slits. In contrast, at the wavelength of the narrow resonance, $I(x)$ shows almost negligible intensity at the slits and two strong maxima in between the slits. These standing-wave SPP modes essentially result from the interference of the two grating-coupled propagating SPP modes, in this case the AM[+1] and AM[–1] modes. Since the nanoslits effectively serve as scattering centers [32], coupling evanescent SPP modes into propagating far-field modes, it is apparent that the radiative damping of the dark mode, with reduced SPP field intensity at the slits, is largely reduced. This qualitative explanation is confirmed by an analysis within a coupled-mode model and by quantitative scattering matrix simulations [11, 99, 100].

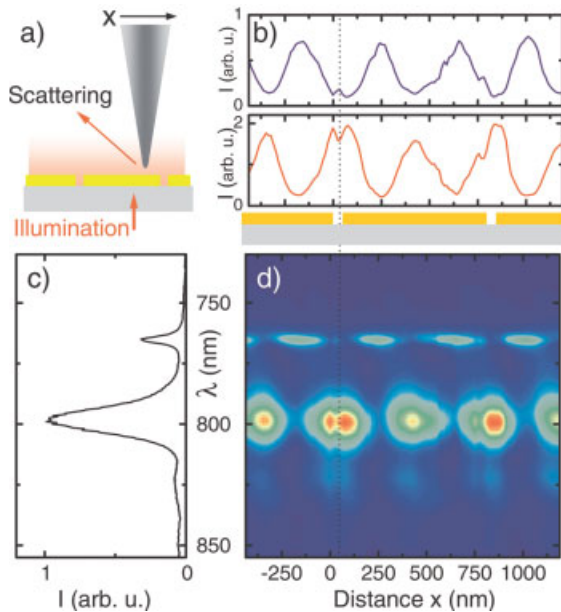


Figure 15 (online color at: www.lpr-journal.org) Spectrally resolved NSOM image of the SPP fields at the metal-air interface of a nanoslit grating with a grating period $a_0 = 750$ nm [11, 33]. The images are recorded in the spectral window around the AM[+1]/AM[−1] crossing. (a) Experimental configuration. An aluminum-coated fiber tip is used to scatter the near fields into the far field. Intensity of the scattered light as a function of position and wavelength. (b) Spatial dependence of the near-field intensity at 766 nm (narrow resonance, blue line) and at 800 nm (broad resonance, red line). (c) Spatially averaged near-field spectrum. (d) Spatially and spectrally resolved near-field image recorded by scanning the tip along the x -axis, perpendicular to the slit axis, at a constant distance of about 10 nm across the sample.

In summary, we have shown that a combination of near-field imaging and coherent ultrafast optics provides detailed insight into the physical mechanism underlying the extraordinarily enhanced transmission through periodic arrays of nano-apertures in metal films. The enhancement results from an interference of light directly passing through the apertures and resonantly excited SPP radiation which is grating scattered into the far field. Details of the linear optical properties of such arrays including the band-gap formation and their effect on the SPP lifetimes are now reasonably well understood. Such nanostructures therefore have developed into important model systems for probing the interaction between SPP modes and various quantum emitters, e.g., excitons in semiconductor nanostructures as described in Sect. 5.

4.2. Nanometer-sized sources

This section demonstrates two new forms of ultrafast nano-optical light and electron sources recently reported in [34–36], which are based on the principles encountered

in the previous sections. The light source is based on SPP excitation on a metal grating followed by SPP propagation on flat metallic surfaces and rescattering at highly curved geometries [34]. The electron source utilizes field enhancement resulting from the SPP localization at sharp metal tips to locally generate few-fs electron pulses via a multi-photon ionization process [35, 36].

4.2.1. Nanometric light source by launching SPPs onto nanotips

An interesting approach to dramatically improve the lateral resolution and simultaneously avoid pulse propagation through fiber probes is scattering SNOM (s-SNOM), in which sharp tips with apical radii down to 2 nm are used as near-field scatterers [24, 25]. However, s-SNOM generally suffers from a strong overall background coming from the far-field illumination. Special modulation as well as detection techniques are then necessary to extract the desired near-field signal from the background [101]. Therefore, in the field of nano-optics there is a high demand for nanometer-sized isolated light emitters to achieve background-free high spatial resolution.

An efficient transformation of traveling delocalized SPPs into highly localized excitations can result in bright illumination of confined volumes and can fulfill the requirements for a background-free, nanometric source of light. Theoretically, tapered structures, such as wedges [102, 103] or cones [104–106], have been proposed which will allow the concentration of SPPs at the apex of these curved convergent geometries [107]. Here, we discuss and demonstrate a novel, local light source by spatially focusing SPPs on nanofabricated, three-dimensionally tapered conical tips with apex radii of a few tens of nanometers. One-dimensional gratings are written onto the shaft of an electrochemically etched tip by focused ion beam milling, more than 10 μm away from the apex [52]. This allows us to easily separate the excitation spot and the tip apex using far-field optics. Illumination of the grating with a broadband femtosecond laser leads to resonant excitation of SPPs [75, 89], which travel to the tip apex, where they are reradiated into the far field. The observed long SPP propagation length on a relatively smooth metal taper with a small radius of curvature at the end allows for realizing a new local light source.

A scanning electron microscope image of a typical nanofabricated metal tip is shown in Fig. 16a. It is based on an electrochemically etched gold tip with a radius of curvature of about 20 nm at the tip apex and an opening angle of 15°. As we have already discussed in the previous section, SPPs can be excited in periodic structures on metallic surfaces via grating coupling. The grating period was chosen to be 750 nm [11, 75] to match the center wavelength of either the 7 fs broadband or a spectrally tunable cw Ti:sapphire laser [108]. The incident light with polarization perpendicular to the grating axis is focused onto the tip shaft to a spot size of about 5 μm at close to normal incidence (Fig. 16a) using a microscope objective. The light

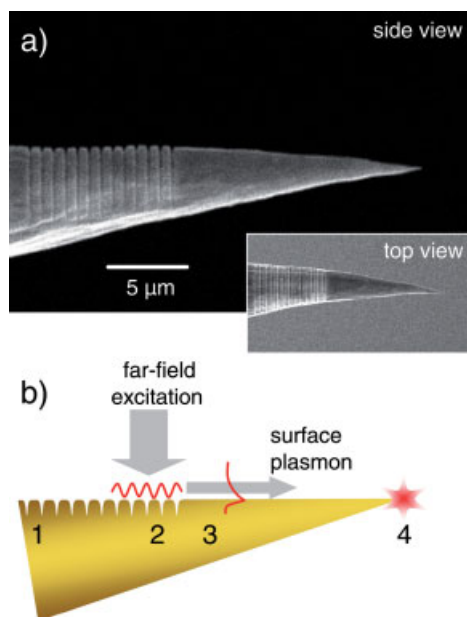


Figure 16 (online color at: www.lpr-journal.org) (a) Scanning electron microscope images of a conical metallic tip with a grating coupler on the shaft prepared by focused ion beam milling. (b) Principle of the non-local excitation of the tip apex. Far-field radiation excites surface plasmon polaritons on the grating, which propagate along the shaft toward the tip apex, where they are reradiated into the far field [34].

scattered from the tip out of the figure plane is collected with a second objective and imaged onto either a video camera or the entrance slit of a spectrometer. Optical microscope images of the light scattered from the tip are recorded for various positions of the illumination spot. Different illumination positions 1 to 4 are marked in Fig. 16b. The scattered light images for these four illumination positions and monochromatic illumination at 755 nm are shown in the image series of Fig. 17. Only when the focus of the illuminating light is moved to position 2, i.e., on the right-hand side of the grating, is an intense signal from the tip end observed. This image clearly shows that SPPs are very efficiently excited at the grating and propagate over a distance of more than $10\ \mu\text{m}$ without strong scattering losses. Finally, they are reradiated into the far field at the apex of the tip. From the comparison of the signal levels a conversion efficiency of 0.1–1% is estimated. This intense radiation from the tip apex is only observed for a polarization of the incident light perpendicular to the grooves, confirming its SPP origin.

By comparing the images corresponding to positions 2 (indirect grating illumination) and 4, in which the tip is directly illuminated, the scattered light is found to be spatially less confined for direct tip illumination. This is a direct signature for the strong field enhancement occurring for SPP localization at the tip apex [35, 109].

The optimum choice of the distance between the grating and the tip apex is a trade-off between the propagation

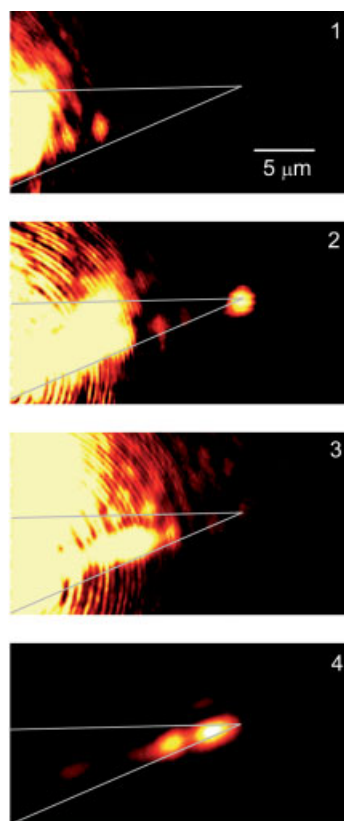


Figure 17 (online color at: www.lpr-journal.org) Series of microscope images recorded for illumination of the tip at the four positions indicated in Fig. 16b. Image 2 demonstrates the efficient non-local excitation of the tip apex via illumination of the grating [34].

losses and the reduction in the background signal due to the scattering. Experimentally, the optimum condition for the tip excitation was found for slightly defocused illumination on the grating which resonantly enhanced the SPP coupling efficiency and was confirmed by spectrally resolving the light scattered from the tip apex under illumination of the grating. In Fig. 18, three scattering spectra are shown for different angles of incidence. The spectra are normalized to the incident laser spectrum and clearly show the resonant behavior of the SPPs. To further support the observations, model calculations have been performed using a scalar discrete dipole model with SPP scattering [110]. The simulated spectra are shown as an inset in Fig. 18. They can nicely reproduce the angle-induced shift in the scattering spectra.

The scattering spectra show line widths of several tens of meV and suggest the possibility of launching SPP wave packets with a pulse duration of a few tens of fs onto the tip shaft. Theoretical results indicate that significant chirp may be acquired by a SPP wave packet upon propagation on such a tapered conical waveguide. It will therefore be interesting to experimentally investigate pulse propagation on such complex conical waveguides.

In conclusion, the possibility of an effective non-local excitation of the apex of a sharp metallic tip by virtue of grating coupling has been demonstrated. Such nanofabricated tips will serve as a useful nanoscale light source in s-SNOM, preventing many of the background scattering problems existing in current s-SNOM setups.

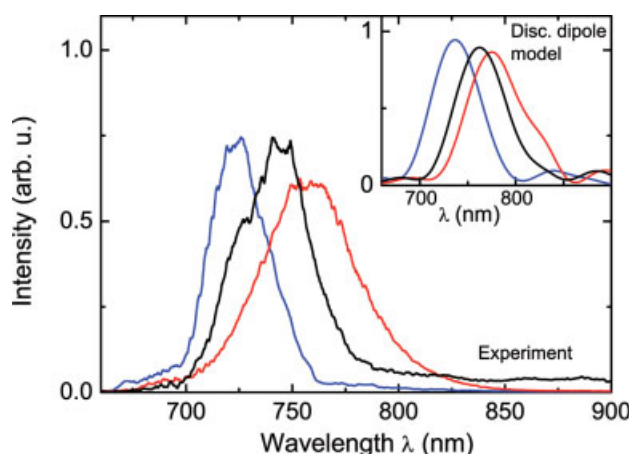


Figure 18 (online color at: www.lpr-journal.org) Recorded scattering spectra from the tip apex for non-local excitation at the grating edge near normal incidence ($\theta \sim 0^\circ$, red) and for two slightly larger angles of incidence of about 1° (black line) and 2° (blue line). The spectra are normalized to the broadband input laser spectrum. A shift and slight broadening of the spectra are observed. A similar behavior is found within a phenomenological discrete dipole model (inset) for angles of incidence of 3.5° (red), 4.5° (black) and 6.5° (blue) [34].

4.2.2. A nanometer-sized femtosecond electron source based on optical field enhancement at metallic nanotips

Femtosecond electron and X-ray diffraction/imaging are emerging techniques that allow for probing the microscopic structural dynamics of molecular and solid-state systems with a spatio-temporal resolution that is unachievable by conventional spectroscopy techniques [15, 16, 19]. Despite substantial recent progress, these experimental techniques are still in an early stage and lots of efforts are currently made to develop the ultrafast electron [111] and X-ray [112] sources which can give the desired temporal resolution. In ultrafast electron diffraction, overcoming the temporal smearing due to Coulomb repulsion is challenging [113, 114]. Therefore, it would be desirable to use individual nanostructures as an isolated source of single electrons with a sub-10-fs response time. For such a purpose, metal nanostructures like sharp gold tips are promising as they offer large optical field enhancements and high damage thresholds.

Here, we discuss the demonstration of an ultrafast electron source generated by illuminating ultra-sharp metal tips with light pulses of sub-10-fs duration. Intense electron emission from a point-like area at the tip apex is observed even in the absence of bias voltages [35, 36].

The experimental setup developed for investigating the electron generation from sharp metal tips is shown in Fig. 19. Light pulses from a Ti:sapphire laser of 7-fs duration are focused to a spot size of about $1.5 \mu\text{m}$ by a reflective Cassegrain microscope objective. An electrochemically etched gold tip with a radius of curvature of about 20 nm mounted on a piezo scanner can be raster

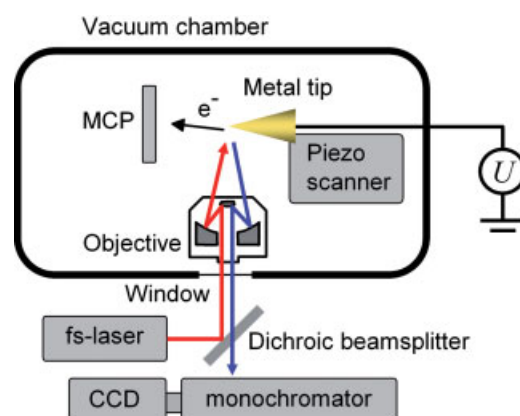


Figure 19 (online color at: www.lpr-journal.org) Experimental setup for the simultaneous detection of electron emission and non-linear light generation from ultra-sharp metal tips. Optical pulses from a fs laser are focused with a Cassegrain mirror objective onto the tip. Both objective and tip are mounted inside a vacuum chamber and the optical pulses are coupled into this chamber through a thin quartz window. The emitted electrons are detected with a micro-channel plate (MCP). An arbitrary bias voltage U can be applied to the tip [33, 35].

scanned through the laser focus. For electron detection, a chevron-type micro-channel plate (MCP) detector is placed opposite to the tip, and voltage pulses from the MCP detector resulting from single-electron events are counted with an electronic discriminator. A variable bias voltage U can be applied to the tip.

The spatial characteristics of the electron generation are studied by probing the electron signal while scanning the tip in the plane perpendicular to the optical axis (y -direction) through the laser focus (Fig. 20). In these images, the electron signal is plotted on a logarithmic intensity scale. When the polarization direction of the incident laser is oriented along the axis of the metal tip (y -direction), an intense electron signal ($> 10^6 e^-/s$) from a $0.5 \times 1 \mu\text{m}^2$ region at the very end of the metal tip is observed at $U = 0$. This spot size is smaller than the illuminating spot size of $1 \times 2 \mu\text{m}^2$, assessed from the simultaneously recorded back-scattered laser light. Rotating the incident polarization to the perpendicular direction, the emission from the tip apex is reduced by more than two orders of magnitude, clearly illustrating the polarization selectivity of the field enhancement promoting the electron generation. A similar polarization dependence was also observed in rather intense second-harmonic generation and two-photon-induced photoluminescence at the tip apex where the electron signal has its maximum. Comparing the electron flux from the tip apex with that from the shaft, a local field enhancement factor is estimated to be 10, which is in good agreement with the theoretically predicted value of ~ 12 for gold tips of similar sharpness.

For investigating the physical mechanism underlying this field-enhanced electron generation, the metal tip is di-

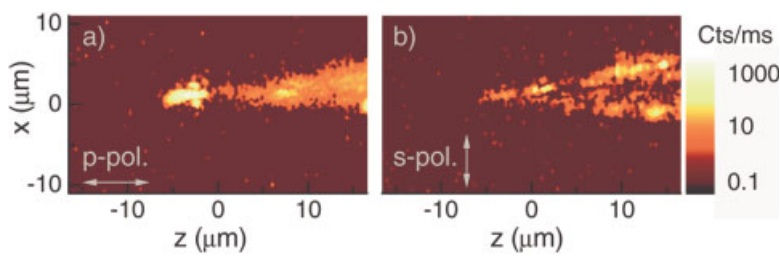


Figure 20 (online color at: www.lpr-journal.org) Electron-generation rate (logarithmic color scale) for an incident polarization parallel (a) and perpendicular (b) to the tip axis oriented along z . For perpendicular polarization, the electron emission from the tip apex is suppressed by more than two orders of magnitude [33, 35].

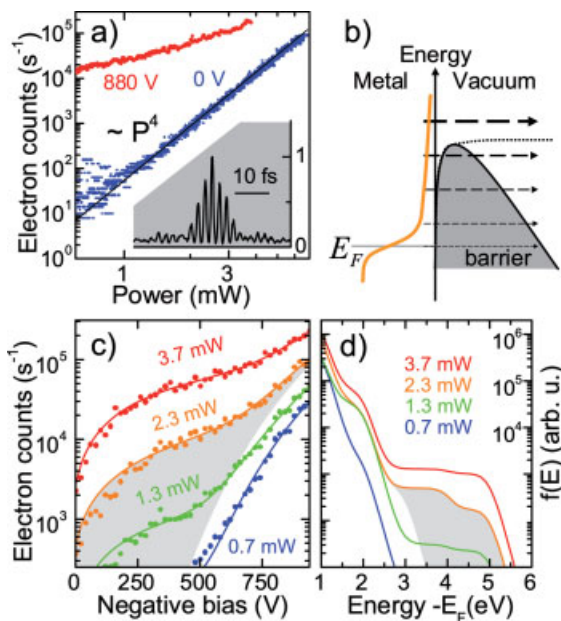


Figure 21 (online color at: www.lpr-journal.org) (a) Power dependence of the electron signal for bias voltages of 0 and 880 V. Inset: interferometric autocorrelation of the laser pulses detected via the electron signal. (b) Illustration of the tunneling model. (c) Voltage dependence of the electron emission for four different incident powers and predicted currents from the associated optically induced non-equilibrium carrier distribution function $f(E)$, plotted in (d) as a function of excess energy above the Fermi energy E_F . [33, 35].

rectly moved into the laser focus and the electron signal is monitored as a function of tip bias voltage and the incident laser power. At zero tip bias, a fourth-order dependence of the electron signal J on the laser power P is observed (Fig. 21a). The inset in Fig. 21a shows the interferometric autocorrelation of the electron signal generated by a pair of phase-locked laser pulses revealing a strong enhancement at zero pulse delay. The incident photon energy of ~ 1.5 eV compared to the gold work function of about 5 eV, the clear fourth-order power dependence and the enhancement at zero pulse delay show directly that the electrons are generated by a highly nonlinear multi-photon ionization process. The bias-voltage dependence (Fig. 21c) also shows that the electrons are generated from a short-lived non-equilibrium carrier distribution function [115–121] and that different parts of this distribution function are emitted depending

on the bias voltage. The generation mechanism changes from one-photon-assisted tunneling at high bias voltages to four-photon-induced emission at zero bias. The tunneling scheme is schematically depicted in Fig. 21b. At low optical powers, the non-equilibrium distribution (Fig. 21d) is well described by a hot Fermi distribution with a carrier temperature of several thousand Kelvin. At the highest powers, however, our experiments give clear evidence that the electrons are emitted from a transient, *non-thermal* electron distribution. This short-lived electron distribution is generated by multi-photon absorption. Since this short-lived non-thermal distribution exists for at most a few tens of femtoseconds, its dominant role for the electron-generation process ensures that the duration of the electron pulses is indeed restricted to the few-fs regime.

The high optical nonlinearity of the electron emission in the absence of a bias voltage makes such nanotips exceptionally sensitive probes for detecting (time-varying) local electromagnetic fields through a modification of the free-electron yield. To explore this potential, a novel tip-enhanced electron-emission microscope (TEEM) [122] was set up. It is based on a mechanically durable tungsten tip in proximity to a nanostructured gold surface (a 100 nm wide groove [11]) and is displayed in Fig. 22a. In order to verify both surface sensitivity and lateral resolution of this setup, the tip and the sample are illuminated by focused 7 fs light pulses and the locally generated electron flux is monitored while raster scanning the sample position relative to the tip in the x - z plane, i.e., perpendicular to the sample surface. The color-coded image of Fig. 22b on the air side of the metal surface represents the local electron signal as a function of the relative tip-sample position. It is evident that the electron signal is strongest when the tip is in the direct vicinity of the sample surface and close to the edges of the groove. An approach curve near a groove edge, Fig. 22c, shows an increase of the electron signal by a factor of ~ 5 within the last 50 nm to the surface. The lateral resolution in the image presented here is certainly better than 40 nm and is limited by the sharpness of the tip and the nanostructure features. The results presented here directly show that the electron signal is predominantly generated in the gap between tip and sample and that the resolution of the microscope is governed by the size of the metal tip and not by the wavelength of the illuminating light. Also, in these experiments, a high-repetition-rate, low-pulse-energy laser source is used to generate the electrons. Hence, the number of electrons per laser pulse is very low, creating mostly only a single electron per pulse. Due to the high, 80-MHz repeti-

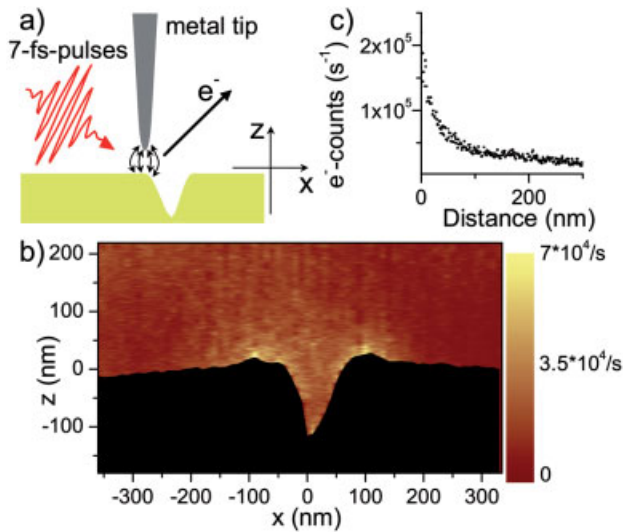


Figure 22 (online color at: www.lpr-journal.org) (a) TEEM setup. The illuminated metal tip is brought close to a nanostructure, and the local electron generation is monitored as the sample position is scanned relative to the tip. (b) Distance-dependent TEEM image of a nanometric groove in a gold surface. The cross section of the groove is given by the dark area and determined by a simultaneous shear-force measurement. (c) Electron signal approach curve near a groove edge [35, 36].

tion rate of the laser, however, the total electron flux is as high as in previous diffraction experiments [15]. Therefore, this new source prevents temporal smearing of the electron pulses due to Coulomb repulsion and thus may be of key importance for obtaining increased, few-fs temporal resolution in time-resolved electron microscopy and diffraction.

The results in this section demonstrate the imaging capabilities of this novel tip-enhanced electron microscope. Its inherent temporal resolution, however, has so far not

yet been explored. It is easily envisaged that such a microscope, when being illuminated with pairs of time-delayed femtosecond pulses, can analyze surface plasmon polariton dynamics near the surfaces of nanostructures with femtosecond or even sub-fs time resolution [123].

4.3. Coherent control of SPP fields on the nanoscale

The control of light propagation and localization on a sub-wavelength scale is one of the key challenges in nanophotonics. By now, it has been well established that adaptive shaping of the phase and amplitude of femtosecond laser pulses can be developed into an efficient tool for the desired manipulation of interference phenomena providing coherent control over various systems [124–127]. In the previous sections, we have already seen that interference phenomena in SPPs give rise to very interesting effects like, e.g., sub- and super-radiative decay of the SPP resonances. In the present section, we briefly discuss results by Aeschlimann *et al.* reporting the overcoming of the diffraction limit in far-field spectroscopy by illuminating nanostructures with actively shaped ultra-short laser pulses [37]. Using adaptive control that combines multi-parameter pulse shaping with a learning algorithm it was possible to demonstrate generation of a user-specified optical near-field distribution. As the near-field response is strongly polarization dependent, polarization shaping of the laser pulses provides a particularly efficient and versatile nano-optical manipulation method [37].

In [37], the optical near field in the vicinity of silver nanostructures (Fig. 23) was tailored through adaptive polarization shaping of femtosecond laser pulses followed by probing of the lateral field distribution by two-photon photoemission electron spectroscopy (PEEM) [128].

Circular silver disks having 180 nm diameter and 30 nm height arranged into three dimers were fabricated by

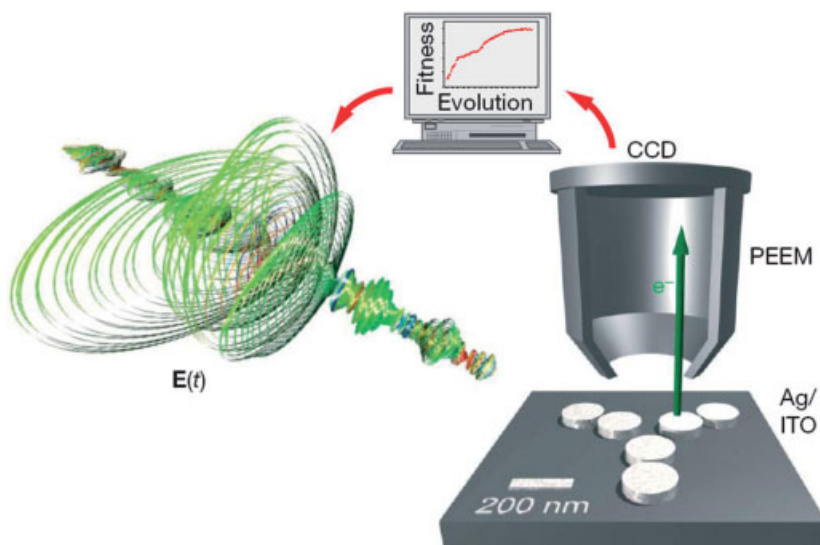


Figure 23 (online color at: www.lpr-journal.org) Experimental scheme for coherent control of nano-optical fields [37]. A polarization shaper for ultra-short laser pulses controls the temporal evolution of the vectorial electric field $\mathbf{E}(t)$ on a femtosecond time scale. These pulses illuminate a planar nanostructure in an ultra-high-vacuum chamber that is equipped with a photoemission electron microscope. The nanostructure consists of six circular Ag islands on an indium-tin oxide (ITO) film and a quartz substrate. A computer-controlled charge-coupled device (CCD) camera records the photoemission image and provides a feedback signal for an evolutionary learning algorithm. Iterative optimization of the pulse-shaper settings leads to an increase in the fitness value and correspondingly allows control over the nano-optical fields.

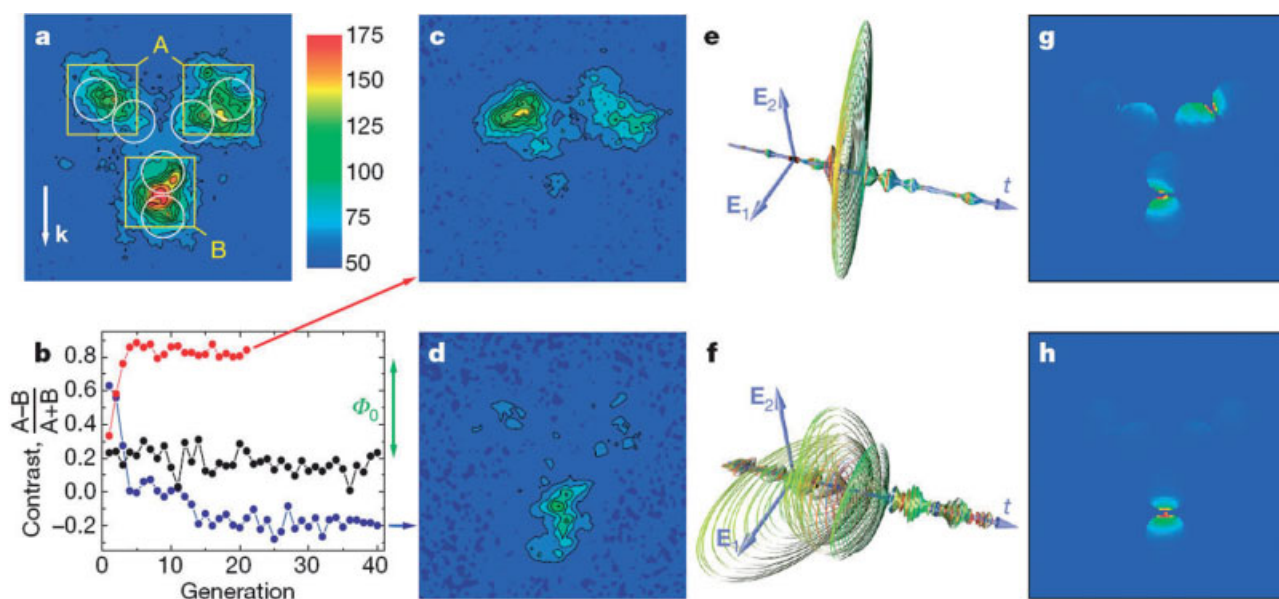


Figure 24 (online color at: www.lpr-journal.org) (a) The experimental photoelectron distribution is displayed on a $1.13 \mu\text{m} \times 1.13 \mu\text{m}$ square for p-polarized excitation of the star-shaped nanostructure with laser pulses at 790 nm [37]. This distribution acts as a reference for the optimization experiments with complex polarization-modulated laser pulses. The color scale bar represents the photoemission yield in arbitrary units with negligible dark events but including the read-out noise of about 50. The white arrow indicates the projected direction of incidence k (incidence angle 65°). The nanostructure positions are marked by white circles and the regions of interest A and B by yellow squares. (b) Adaptive optimization of the A/B photoemission ratio leads to increased (red) and decreased (blue) contrast of electron yields from the upper and lower regions as compared to unshaped laser pulses recorded as a reference (black). For comparison, the range of contrast variation achieved by non-adaptive single-parameter scanning of the spectrally constant phase offset between the two pulse-shaper polarization components (green arrow) is smaller and does not provide the same degree of control. (c) The experimental PEEM image after adaptive A/B maximization using complex polarization-shaped laser pulses shows predominant emission from the upper region. (d) Photoemission after A/B minimization is concentrated in the lower region. (e, f) The optimal laser pulses, as experimentally characterized, display complex temporal electric-field evolution for the maximization (e) and minimization (f) objectives. E_1 and E_2 indicate the two field components that are phase modulated in the polarization pulse shaper in the first and second LCD layers, respectively. They are at $\pm 45^\circ$ angles with respect to p-polarization. The overall time window shown is 2 ps. (g, h) The simulated two-photon photoemission pattern for the experimental pulse shapes in the cases of A/B maximization (g) and minimization (h) qualitatively confirm the experimentally demonstrated nano-optical field control.

electron-beam lithography on an indium-tin oxide film grown on a quartz substrate. The experimental photoelectron distribution for this sample is shown in Fig. 24a when excited by p-polarized laser pulses at 790 nm. This distribution acts as a reference for the optimization experiments. The color scale bar represents the photoemission yield in arbitrary units with negligible dark events. The white arrow indicates the projected direction of the incident wave vector (incidence angle 65°). The nanostructure positions are marked by white circles and the regions of interest A and B by yellow squares. The incident pulse parameters are altered so that the PEEM signal from either region A or region B is maximized (Fig. 24b) as compared to the unshaped laser pulses recorded as a reference. The experimental PEEM images after adaptive A/B maximization using complex polarization-shaped laser pulses are shown in Fig. 24c and d, respectively. The orientations of the electric field vector of the incident pulse as a function of time that give maximum photoemission either from the top (A) or the bottom region (B) are shown in Fig. 24e and f, respec-

tively. The simulated two-photon photoemission patterns (Fig. 24g and h) for the experimental pulse shapes are also shown with satisfactory matching between observed and simulated images.

The technique described above demonstrates mapping of photoemission patterns governed by local optical near fields with nanometer resolution and shows that the optical near field can be manipulated on a subdiffraction length scale. The experimental realization of coherent control using adaptive optics opens up a number of perspectives in coherent control, nano-optics and nonlinear spectroscopy [47, 129]. The technique can also be used to create an ultrafast nano-optical switch or multiplexer delivering ‘packets’ of electromagnetic energy at desired locations below the diffraction limit, which will be useful for many applications in nano-optics [130].

Other variations of similar techniques in which photoelectron emission microscopy is combined with attosecond streaking spectroscopy have also been proposed [38]. The proposed experimental setup is shown in Fig. 25. The sam-

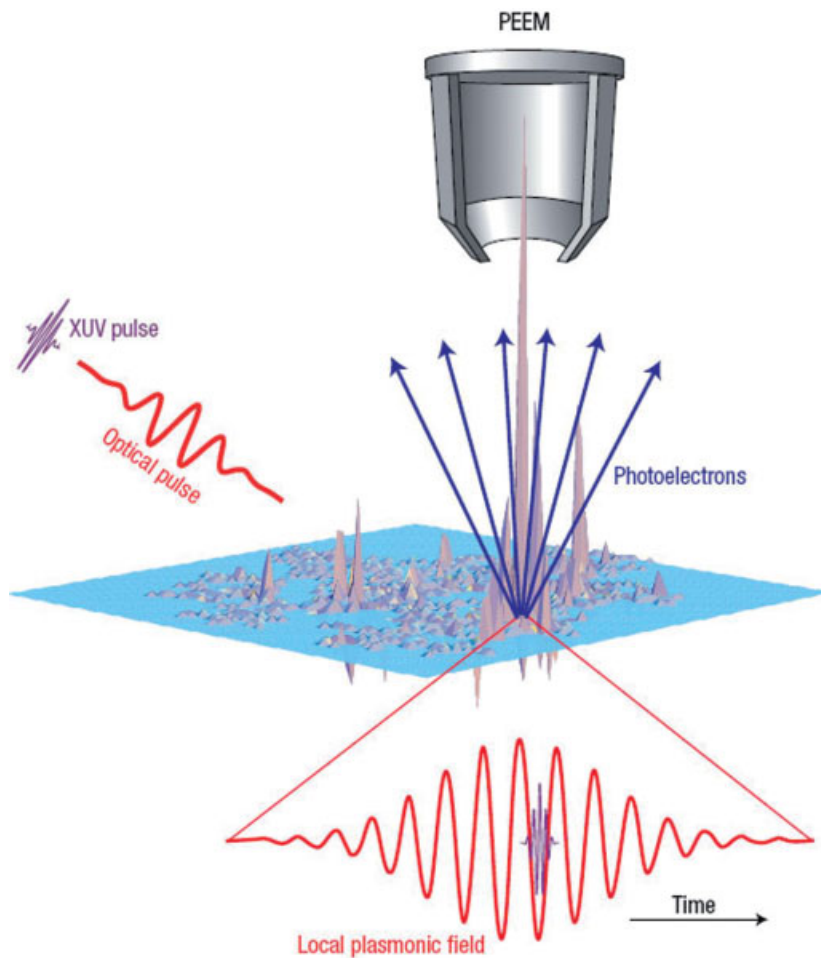


Figure 25 (online color at: www.lpr-journal.org) Schematic of an attosecond nanoplasmonic-field microscope [38]. The investigated nanosystem is shown in a plane denoted in light blue. Instantaneous local fields, which are excited by the optical pulse, are shown as a three-dimensional plot. The local optical field at a point of the maximum field (‘hottest spot’) is shown as a function of time by a red waveform, enhanced with respect to the excitation field. The application of an XUV pulse is shown by a violet waveform that is temporally delayed with respect to the excitation field. The XUV excitation causes the emission of photoelectrons shown by the blue arrows, which are accelerated by the local plasmonic potential. They are detected with spatial and energy resolution by a PEEM.

ple will be illuminated by an ultrafast pulse of light creating a local field distribution around it. A delayed XUV pulse will then interact with this field to cause the emission of the photoelectrons, which will be detected as a function of the delay between the two optical pulses. When being realized, this technique will provide direct, non-invasive access to nanoplasmonic dynamics with nanometer-scale spatial resolution and temporal resolution on the order of 100 attoseconds.

5. SPP-exciton interactions in metal-semiconductor hybrid nanostructures

So far we have seen that SPPs can be used in a variety of situations, e.g., to generate higher field intensities [35, 36] or localized sources [34, 35], as well as in novel spectroscopy [37] and microscopy [36, 38] techniques to achieve high spatio-temporal resolution. It should be noted, however, that SPPs are not purely electromagnetic fields but are mixed electron-photon modes, generated by collective oscillations of free electrons in metals [33]. This mixing of electron and photon modes results in the short in-plane wavelengths of SPP and thus is the key to localizing light on

the nanoscale. Another consequence of this mode mixing, however, is the strong non-radiative damping of SPP modes and the corresponding short SPP lifetimes of typically a few tens of femtoseconds. Overcoming this strong damping therefore is an important future goal in metal-based nano-optics. One conceptual possibility for reaching this goal is to combine metal nanostructures with gain media, e.g., semiconductor or molecular nanostructures, in order to reduce the SPP losses and eventually achieve SPP amplification and lasing [131, 132]. The concept of a SPP laser or SPASER (surface plasmon amplification using stimulated emission of radiation) has recently been introduced by Bergman and Stockman [131] and is a fundamentally different way of exciting giant local optical fields.

A SPASER is a metal nanosystem that supports SPP eigenmodes and is surrounded by an active medium of population-inverted emitters like semiconductor quantum dots or dye molecules in a solution. Like the laser active medium, the SPASER active medium can be pumped optically, electrically or chemically and its energy is transferred non-radiatively to a resonant metal structure [131, 132]. This scheme has a great advantage in spectroscopy compared to the conventional illumination sources. As the SPASER can be made purely non-radiative, it is essen-

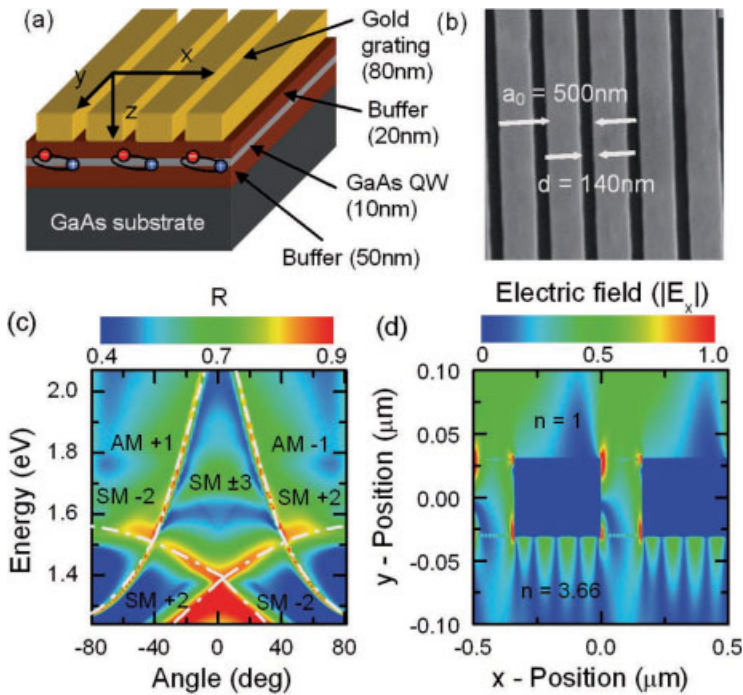


Figure 26 (online color at: www.lpr-journal.org) (a) Schematic of the metal-semiconductor hybrid structure consisting of a gold nanoslit grating deposited on a GaAs QW. (b) SEM image of the gold grating with $a_0 = 500$ nm, $d = 140$ nm and $h = 80$ nm. (c) Calculated angle-resolved far-field reflectivity spectra for different AM and SM SPP resonances. Dispersion relations for different AM and SM SPP resonances are indicated as dash-dotted lines. (d) Calculated spatial distribution of the normal electric field E_x for $E_{ex} = 1.517$ eV and $\theta = 38^\circ$, near the crossings of the SM[+2], SM[-3] and AM[-1] SPP resonances [39].

tially a background-free source and can greatly enhance the scope of SPP-based ultrafast nano-optical techniques.

A crucial step towards the design and optimization of SPASERS is to understand the microscopic physical processes underlying the optical interactions between SPPs and quantum emitters serving as the gain material. It is well known that the radiative coupling between an emitter and its electromagnetic environment significantly modifies in particular the spontaneous emissive properties of the emitter [133–137]. Many groups have investigated similar interactions in close proximity of metallic structures [138, 139]. Various experimental [79, 140, 141] and theoretical [138, 142] studies have shown an enhancement in the luminescence yield as well as a reduction of the excitonic lifetime of a QW when placed close to a metallic nanostructure due to its coupling to SPPs. Other reports, however, show a suppression of luminescence in the proximity of a metal surface [143, 144]. The discussion of these results has partly remained controversial because the existing experiments gave limited insight into the microscopic nature of the coupling. Hence, the interaction between a metallic nanostructure and a quantum emitter is not yet fully understood. One of the most direct ways to probe this interaction is to study the normal mode splitting between QW excitons and SPPs. In this section, we present results of our recent experiment probing the interaction between excitons and SPPs [39].

We investigate a multi-layered metal-semiconductor hybrid structure consisting of a gold grating [11, 100] deposited on a GaAs QW. A schematic illustration of the sample cross section and a scanning electron microscope image of the top surface are shown in Figs. 26a and b, respectively. As discussed in Sect. 4.1, angle-dependent re-

flectivity spectra of such nanoslit arrays reveal excitation of different AM and SM resonances. This is also illustrated in the simulations shown in Fig. 26c. The hybrid structure parameters are chosen similar to our sample and the spectra have been calculated using a full vectorial diffraction model [99, 100] by assuming a spatially homogeneous refractive index $n_s = 3.66$ of the semiconductor layers. The spectra indicate that at excitation energies of ~ 1.5 eV, i.e., around the exciton resonance of a 10 nm GaAs QW, and at an incidence angle $\theta = 40^\circ$, three different SPP modes – AM[-1], SM[+2] and SM[-3] – are almost in resonance leading to an efficient coupling among these modes via the light transmitted through the nanoslits [11, 100]. In Fig. 26d, the spatial distribution of the electric field component E_x perpendicular to the slit axis is shown for illumination by a p-polarized monochromatic plane wave with $E_{ex} = 1.517$ eV, incident at $\theta = 38^\circ$. This is close to the crossing of the SM[-3], SM[+2] and AM[-1] SPP resonances. The calculations indeed reveal the formation of coupled SPP modes with spatially localized field intensities at both the AM and SM interfaces. The light hole (LH) and heavy hole (HH) exciton resonances in a 10 nm wide GaAs QW at 10 K occur at 1.554 eV and 1.546 eV, respectively. In our sample, the 500 nm grating period and 140 nm slit width are chosen so that these QW resonances match very well with the coupled SPP mode arising from the overlap of AM and SM SPP modes [39].

The sample is illuminated in the energy range 1.503–1.569 eV with a weakly focused p-polarized beam from a tunable cw Ti:sapphire laser. High-resolution, angle-resolved linear reflectivity spectra are recorded at a temperature of 10 K in the range 26–44° with an angular resolution of 0.2° and a spectral resolution of 0.2 meV (Fig. 27a).

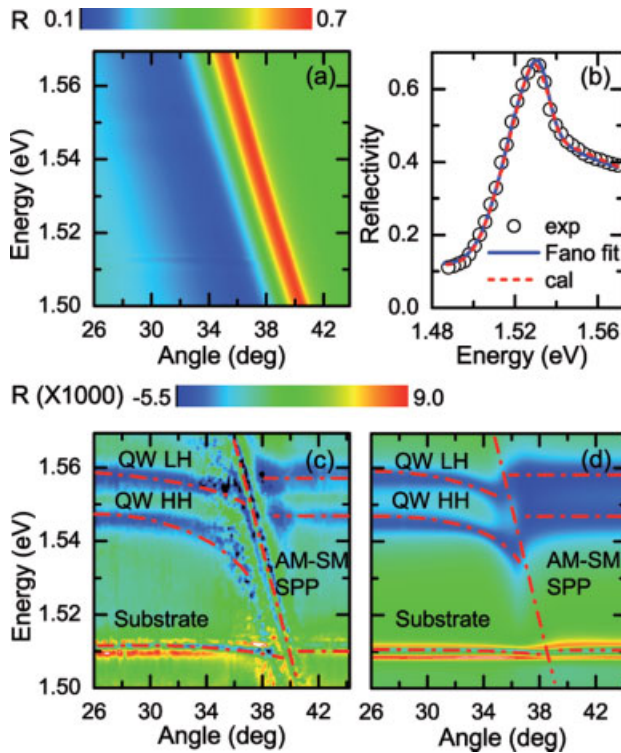


Figure 27 (online color at: www.lpr-journal.org) (a) Angle-resolved reflectivity spectra ($T = 10$ K) of the hybrid structure. The dominant feature is the resonance resulting from the coupling of the AM[−1], SM[+2] and SM[−3] SPP modes. (b) Spectrum at $\theta = 38^\circ$ (open circles) together with simulations based on the Fano (blue solid line) and the coupled-oscillator model (red dashed line). (c) Reflectivity spectra obtained after subtracting the SPP contribution from (a). The spectra reveal a clear shift of the QW HH and LH resonances. (d) Spectra obtained from the coupled-oscillator model. Red dash-dotted lines indicate the SPP and QW HH and LH dispersions, respectively [39].

The spectra are almost entirely dominated by the strong reflectivity peak of the SPP resonance resulting from the coupling among the AM[−1], SM[+2] and SM[−3] modes. This resonance is highly dispersive and is essentially unaffected by the presence of the QW. Very faint features from the QW and GaAs substrate (at 1.512 eV) resonances are also visible. As expected, the QW signature is weak since most of the incident light is simply reflected off the metal grating. To obtain more information about the QW dispersion, the contribution from the coupled SPP mode is fitted (Fig. 27b) to the now well-established Fano line shape (Sect. 4.1) and is subtracted from the data [11, 32, 90]. Thus-obtained spectra in the energy range where SPP and exciton coexist are shown in Fig. 27c and clearly show the formation of coupled modes. Significant bending in the QW LH and HH resonances close to the SPP–exciton crossing together with a change in the broadening are observed. As the substrate lies more than 50 nm below the grating, the substrate resonance is only marginally affected by SPPs.

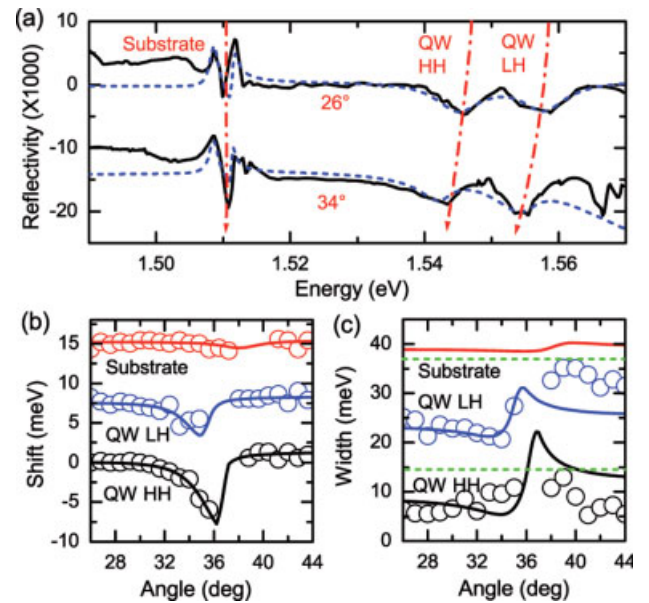


Figure 28 (online color at: www.lpr-journal.org) (a) Experimental (black solid lines) and simulated (blue dashed lines) reflectivity spectra at $\theta = 26^\circ$ and 34° , respectively. The red dash-dotted lines are guides to the eye. (b,c) Experimental (open circles) and simulated (lines) energy shifts (b) and line widths (c) of the LH (blue), HH (black) and substrate (red) excitonic resonances as a function of angle θ . The LH and substrate transitions are vertically shifted for clarity. In (c), the green dashed lines mark the new reference positions [39].

In order to explain the coupling between excitons and SPPs, a phenomenological model based on three coupled oscillators [145, 146] is used, in which the SM plasmon, AM plasmon and each of the excitonic resonances are treated as Lorentzian oscillators. The calculated QW dispersion is illustrated in Fig. 27d as well as in Fig. 28a and is found to be in very good agreement with the observed one. Fig. 28b and c respectively show the measured and calculated energy shift and the spectral width of the coupled modes as a function of angle. Considering the simplicity of our model, the results are in excellent agreement with our observations. For the HH exciton, our results show a significant shift of ~ 7 meV and a surprisingly large increase in the radiative damping by ~ 4 meV. This pronounced dipolar coupling between QW exciton and evanescent SPP field [147], seen here for the first time in a metal-semiconductor hybrid system [39], shows that the metal grating serves as an efficient directional outcoupler for the QW emission. This effect would allow us to greatly enhance the luminescence yield of systems which are strongly non-radiatively damped, e.g., carbon nanotubes, by converting predominantly non-radiative damping into radiative damping.

In conclusion, we have investigated the coherent interaction between quantum well excitons and surface plasmon polaritons in a novel hybrid metal-semiconductor nanostructure. This coupling gives rise to spectral shifts of the

exciton resonance and to a surprising increase in the radiative exciton damping. Our results present a quantitative measure of the coupling strength and show that couplings as large as 50 meV can be reached in samples with optimized geometries. Due to the large optical nonlinearities of QW excitons, such a strong exciton-SPP coupling is of considerable interest for various future applications. It may be beneficial for enhancing the quality factor of metallic nanoresonators by SPP amplification [131, 132], eventually result in SPP lasing or help to transfer quantum information over mesoscopic distances.

6. Summary

The experimental techniques and results presented in the previous sections describe some of the recent progress in 'ultrafast nano-optics' made in the laboratories of the authors and other researchers.

We have shown various applications of such new ultra-high temporal and spatial resolution optical techniques, specifically the coherent manipulation of the nonlinearity of a single quantum dot on a subpicosecond time scale. The successful demonstration of Rabi oscillations in a single quantum dot and in a pair of two dipole-coupled quantum dots proves the capabilities of such techniques in probing and manipulating the dynamics of individual electrons in a semiconductor environment. Various future applications of such techniques in quantum information processing are foreseen.

We also tried to show that the linear optical properties of metallic nanostructures such as plasmonic crystals are now much better understood, partly due to the new information gained by combining temporally and spatially resolved spectroscopy [11, 33]. In particular, periodic nanoslit and nanohole arrays have developed into important model structures for studying the optical properties of plasmonic crystals. This improved knowledge may be crucial for exploring the nonlinear optical properties of new hybrid structures consisting of metals and optical gain media, e.g., metal/semiconductor or metal/polymer complexes, where new phenomena such as surface plasmon polariton amplification or lasing are expected. The results of our recent experiments in this direction performed on metal-semiconductor hybrid structures [39] along with other coherent control techniques [37, 38], which allow field manipulation on the nanoscale, have been presented.

The field localization at metallic nanostructures gives rise to highly localized linear and nonlinear optical effects. We have discussed novel nanosources resulting from both of these effects [34, 35]. A prominent example is second-harmonic generation and electron emission from metal nanotips, which allows for creating nanometer-sized isolated light or electron sources with dimensions down to the 10 nm range [35, 36]. Even though the time structure of the emitted electron burst has not yet been fully characterized, the experiments indicate that it is possible to generate electron pulses with a pulse duration of a few femtoseconds or

even below. Various applications can be foreseen for such a nanometer-sized femtosecond electron source, e.g., in tip-enhanced electron microscopy (TEEM) or in ultrafast electron-diffraction experiments. At present, the time resolution in such experiments is limited to several hundreds of fs, partly due to the Coulomb repulsion of electron bunches produced at kHz repetition rates. In the field-enhanced emission from metal nanotips discussed here, high repetition rate laser sources are used, creating mostly only a single electron per pulse and possibly resulting in greatly increased temporal resolution.

It will be interesting to explore the high spatio-temporal resolution of this new microscope for probing the coherent ultrafast surface plasmon polariton dynamics in metallic and metal-semiconductor nanostructures. From our preliminary measurements on the interaction between SPPs and QWs discussed in Sect. 5, such hybrid structures seem very promising for various applications, in particular SPP amplification and lasing, but also for various ultrafast switching applications. It therefore seems appealing to probe their dynamics with improved temporal resolution. Such studies may also permit us to directly probe the time structure of the nanosized electron pulses.

Acknowledgements One of us (P. V.) wishes to thank the Alexander von Humboldt Foundation and the Schlumberger Foundation for financial support. We also greatly acknowledge financial support by the Deutsche Forschungsgemeinschaft, the European Union and the Korea Foundation for International Cooperation of Science and Technology (Global Research Lab programme).

Most of the experiments reported in Sects. 3–4.2 have been performed while some of us (C. R., R. P., and C. L.) worked at the Max-Born-Institut in Berlin in the Department C ('Nonlinear Processes in Condensed Matter') headed by Thomas Elsässer. We wish to greatly thank Thomas Elsässer for continuous support of this work. We also would like to thank Tobias Günther, Kerstin Müller and Thomas Unold for their important contributions to the work reviewed in Sect. 3. High-quality semiconductor samples for these studies have been provided by the group of Andreas D. Wieck (Ruhr-Universität Bochum). We thank M. Glanemann, V. M. Axt and T. Kuhn from the University of Münster for theoretical support and stimulating discussions. We thank D. J. Park, K. G. Lee, J. E. Kihm and Dai-Sik Kim from Seoul National University, Korea, as well as G. Stibenz, APE Berlin, and G. Steinmeyer, MBI Berlin, for their important contributions to some of the experiments in Sect. 4. We also thank Q. H. Park, Korea University, Seoul, Korea for many discussions and theoretical support. We look forward to continuing these collaborations. Some of the samples in Sect. 4 have been fabricated in the Korea Research Institute of Standards and Science, Taejeon, Korea, in the group of J. Kim. We wish to thank M. Albrecht from the Institut für Kristallzüchtung, Berlin, for fabricating the nanostructured tips presented in Sect. 4.2. The semiconductor-metal hybrid structures studied in Sect. 5 have been fabricated at the University of Arkansas, Fayetteville, USA, in the group of G. Salamo and in the group of E. Johnson at the University of North Carolina, Charlotte, USA. We wish to particularly thank Y. I. Mazur, Vas. Kunets and G. Salamo for their invaluable contributions to this ongoing work.



Parinda Vasa, born in Mumbai (Bombay), India, in 1977, studied physics at the Indian Institute of Technology in Bombay. She received a Ph. D. in physics from Tata Institute of Fundamental Research, India, in 2006. During her Ph. D., she studied optical properties of semiconductor nanoparticle thin films. In the same year, she received a fellowship from the Alexander von Humboldt Foundation, Germany, and later in 2008 the 'Faculty for the Future' fellowship from the Schlumberger Foundation to conduct research in the theoretical physics group led by Erich Runge at the Technical University of Ilmenau and in the 'Ultrafast Nano-Optics' group led by Christoph Lienau at Carl von Ossietzky University, Oldenburg, Germany. Here, her research is focused on investigating novel metal–semiconductor plasmonic structures using nano-optics and ultrafast spectroscopy techniques. Her colleagues and herself have succeeded in observing strong ultrafast optical interactions between metals and semiconductors on the nanoscale in hybrid nanostructures. For her research work she was awarded a Young Scientist Medal by the Indian National Science Academy (INSA) in 2007.



Claus Ropers, born in 1977, studied physics at the University of Göttingen and the University of California at Berkeley until 2003. At the Max Born Institute in Berlin, he performed his doctoral work on ultrafast optical excitations in metallic nanostructures. He received a Ph. D. from the Humboldt University in Berlin in 2007 and was awarded the Carl Ramsauer Prize 2008 for his dissertation. He is currently leading the research group 'Nano-Optics and Ultrafast Dynamics' at the University of Göttingen as a tenure track junior professor.



Robert Pomraenke was born in Berlin, Germany in 1978. He studied physics at the Humboldt University in Berlin, finishing in 2004 with a diploma thesis about optical and electrical properties in self-organized InAs quantum wires. He then joined the Max Born Institute in Berlin to perform his Ph. D. work under the supervision of Christoph Lienau. In 2006, he moved to Oldenburg to join the newly established 'Ultrafast Nano-Optics' group at the Carl von Ossietzky University. During his Ph. D., he studied the optical properties of different new semiconductor nanostructures such as quantum dots and carbon nanotubes. Here, performing pioneering two-photon spectroscopy experiments, he

could contribute to establishing the existence of excitons in carbon nanotubes. In Oldenburg, his research is focused on studying dipolar couplings of excitons and surface plasmon polaritons in novel metal–semiconductor as well as metal–dye hybrid nanostructures.



Christoph Lienau, born in 1963, studied physics at the University of Göttingen, Germany. In 1992, he received a Ph. D. in physical chemistry for his research on the dynamics of elementary chemical reactions in molecular clusters. He then accepted a postdoctoral fellowship of the German Science Foundation and worked for two years as a Research Fellow in the group of Ahmed H. Zewail (Nobel prize in chemistry, 1999) at California Institute of Technology, Pasadena, USA, studying femtosecond dynamics of small molecules in solution. In 1995, he moved to Berlin, Germany, to become a member of the scientific staff of the newly founded Max Born Institute in the department of Thomas Elsaesser. At MBI, he initiated a research activity in ultrafast nano-optics, pioneering low-temperature and ultrafast near-field spectroscopy techniques and their applications to nanospectroscopy. In 2006, he became a full professor in physics at the University of Oldenburg. Since 2007, he has been the Vice-Director of the Institute of Physics in Oldenburg. He has published more than 100 papers in refereed international journals and has given more than 60 invited and plenary talks at major international conferences. He holds four patents and is a member of the German Physical Society, the Materials Research Society and the Optical Society of America. His current research interest focuses on nano-optics and ultrafast spectroscopy.

References

- [1] M. Hentschel, R. Kienberger, Ch. Spielmann, G. A. Reider, N. Milosevic, T. Brabec, P. Corkum, U. Heinzmann, M. Drescher, and F. Krausz, *Nature* **414**, 509 (2001).
- [2] M. Dantus, R. M. Bowman, and A. H. Zewail, *Nature* **343**, 737 (1990).
- [3] C. Waschke, H. G. Roskos, R. Schwedler, K. Leo, H. Kurz, and K. Kohler, *Phys. Rev. Lett.* **70**, 3319 (1993).
- [4] J. Faist, F. Capasso, D. L. Sivco, C. Sirtori, A. L. Hutchison, and A. Y. Cho, *Science* **264**, 553 (1994).
- [5] G. Chen, N. H. Bonadeo, D. G. Steel, D. Gammon, D. S. Katzer, D. Park, and L. J. Sham, *Science* **289**, 1906 (2000).
- [6] C. J. Brabec, G. Zerza, G. Cerullo, S. De Silvestri, S. Luzzati, J. C. Hummelen, and S. Sariciftci, *Chem. Phys. Lett.* **340**, 232 (2001).
- [7] T. Q. Nguyen, J. J. Wu, V. Doan, B. J. Schwartz, and S. H. Tolbert, *Science* **288**, 652 (2000).

- [8] X. Hu and K. Schulten, *Phys. Today* **28** (1997).
- [9] T. W. Ebbesen, H. J. Lezec, H. F. Ghaemi, T. Thio, and P. A. Wolff, *Nature* **391**, 667 (1998).
- [10] W. L. Barnes, A. Dereux, and T. W. Ebbesen, *Nature* **424**, 824 (2003).
- [11] C. Ropers, D. J. Park, G. Stibenz, G. Steinmeyer, J. Kim, D. S. Kim, and C. Lienau, *Phys. Rev. Lett.* **94**, 113901 (2005).
- [12] P. B. Corkum and F. Krausz, *Nature Phys.* **3**, 381 (2007).
- [13] M. Merano, S. Sonderegger, A. Crottini, S. Collin, P. Renucci, E. Pelucchi, A. Malko, M. H. Baier, E. Kapon, B. Deveaud, and J. D. Ganiere, *Nature* **438**, 479 (2005).
- [14] V. A. Lobastov, J. Weissenrieder, J. Tang, and A. H. Zewail, *Nano Lett.* **7**, 2552 (2007).
- [15] B. J. Siwick, J. R. Dwyer, R. E. Jordan, and R. J. D. Miller, *Science* **302**, 1382 (2003).
- [16] H. Ihee, V. A. Lobastov, U. M. Gomez, B. M. Goodson, R. Srinivasan, C. Y. Ruan, and A. H. Zewail, *Science* **291**, 5503 (2001).
- [17] C. Rose-Petruck, R. Jimenez, T. Guo, A. Cavalleri, C. W. Siders, F. Raksi, J. A. Squier, B. C. Walker, K. R. Wilson, and C. P. J. Barty, *Nature* **398**, 310 (1999).
- [18] C. W. Siders, A. Cavalleri, K. Sokolowski-Tinten, C. Toth, T. Guo, M. Kammler, M. H. von Hoegen, K. R. Wilson, D. von Linde, and C. P. J. Barty, *Science* **286**, 1340 (1999).
- [19] M. Bargheer, N. Zhavoronkov, Y. Gritsai, J. C. Woo, D. S. Kim, M. Woerner, and T. Elsaesser, *Science* **306**, 1771 (2004).
- [20] B. Hecht and L. Novotny, *Principles of Nano-Optics* (Cambridge University Press, Cambridge, 2005).
- [21] M. Ohtsu, K. Kobayashi, and T. Kawazoe, *Principles of Nanophotonics* (Taylor and Francis, Florida, 2007).
- [22] E. Betzig and J. K. Trautman, *Science* **257**, 189 (1992).
- [23] E. Betzig, J. K. Trautman, T. D. Harris, J. S. Weiner, and R. L. Kostelak, *Science* **251**, 1468 (1991).
- [24] F. Zenhausern, Y. Matin, and H. K. Wickramasinghe, *Science* **269**, 1083 (1995).
- [25] B. Knoll and F. Keilmann, *Nature* **399**, 134 (1999).
- [26] T. Guenther, V. Emiliani, F. Intonti, C. Lienau, T. Elsaesser, R. Nötzel, and K. H. Ploog, *Appl. Phys. Lett.* **75**, 3500 (1999).
- [27] C. Lienau, *Philos. Trans. R. Soc. Lond. A* **362**, 861 (2004).
- [28] T. Guenther, C. Lienau, T. Elsaesser, M. Glanemann, V. M. Axt, T. Kuhn, S. Eshlaghi, and A. D. Wieck, *Phys. Rev. Lett.* **89**, 057401 (2002).
- [29] T. Unold, K. Mueller, C. Lienau, T. Elsaesser, and A. D. Wieck, *Phys. Rev. Lett.* **92**, 157401 (2004).
- [30] T. Unold, K. Mueller, C. Lienau, T. Elsaesser, and A. D. Wieck, *Phys. Rev. Lett.* **94**, 137404 (2005).
- [31] S. C. Hohng, Y. C. Yoon, D. S. Kim, V. Malyarchuk, R. Müller, C. Lienau, J. W. Park, K. H. Yoo, J. Kim, H. Y. Ryu, and Q. H. Park, *Appl. Phys. Lett.* **81**, 3239 (2002).
- [32] D. S. Kim, S. C. Hohng, V. Malyarchuk, Y. C. Yoon, Y. H. Ahn, K. J. Yee, J. W. Park, J. Kim, Q. H. Park, and C. Lienau, *Phys. Rev. Lett.* **91**, 143901 (2003).
- [33] C. Ropers, T. Elsaesser, G. Cerullo, M. Zavelani-Rossi, and C. Lienau, *New J. Phys.* **9**, 397 (2007).
- [34] C. Ropers, C. C. Neacsu, T. Elsaesser, M. Albrecht, M. B. Raschke, and C. Lienau, *Nano Lett.* **7**, 2784 (2007).
- [35] C. Ropers, D. R. Solli, C. P. Schulz, C. Lienau, and T. Elsaesser, *Phys. Rev. Lett.* **98**, 043907 (2007).
- [36] H. Batelaan and K. Uiterwaal, *Nature* **446**, 500 (2007).
- [37] M. Aeschlimann, M. Bauer, D. Bayer, T. Brixner, F. J. G. de Abajo, W. Pfeiffer, M. Rohmer, C. Spindler, and F. Steeb, *Nature* **446**, 301 (2007).
- [38] M. I. Stockman, M. F. Kling, U. Kleineberg, and F. Krausz, *Nature Photon.* **1**, 539 (2007).
- [39] P. Vasa, R. Pomraenke, S. Schwieger, Yu. I. Mazur, V. S. Kiselev, P. Srinivasan, E. Johnson, J. E. Kihm, D. S. Kim, E. Runge, G. Salamo, and C. Lienau, *Phys. Rev. Lett.* **101**, 116801 (2008).
- [40] R. Müller and C. Lienau, *Appl. Phys. Lett.* **76**, 3367 (2000).
- [41] K. Matsuda, T. Saiki, S. Nomura, M. Mihara, and Y. Aoyagi, *Appl. Phys. Lett.* **81**, 2291 (2002).
- [42] B. A. Nechay, U. Siegner, F. Morier-Genoud, A. Schertel, and U. Keller, *Appl. Phys. Lett.* **74**, 61 (1999).
- [43] B. A. Nechay, U. Siegner, M. Achermann, H. Bielefeldt, and U. Keller, *Rev. Sci. Instrum.* **70**, 2758 (1999).
- [44] M. Labardi, M. Zavelani-Rossi, D. Polli, G. Cerullo, and M. Allegrini, *Appl. Phys. Lett.* **86**, 031105 (2005).
- [45] C. Lienau, A. Richter, and T. Elsaesser, *Appl. Phys. Lett.* **69**, 325 (1996).
- [46] L. Novotny, R. X. Bian, and X. S. Xie, *Phys. Rev. Lett.* **79**, 645 (1997).
- [47] E. J. Sánchez, L. Novotny, and X. S. Xie, *Phys. Rev. Lett.* **82**, 4014 (1999).
- [48] A. Bouhelier, M. Beversluis, A. Hartschuh, and L. Novotny, *Phys. Rev. Lett.* **90**, 013903 (2003).
- [49] J. Steidtner and B. Pettinger, *Phys. Rev. Lett.* **100**, 236101 (2008).
- [50] A. Hartschuh, E. J. Sánchez, X. S. Xie, and L. Novotny, *Phys. Rev. Lett.* **90**, 095503 (2003).
- [51] R. Hillenbrand, T. Taubner, and F. Keilmann, *Nature* **418**, 159 (2002).
- [52] C. C. Neacsu, G. Steudle, and M. B. Raschke, *Appl. Phys. B* **80**, 295 (2005).
- [53] H. G. Frey, S. Witt, K. Felderer, and R. Guckenberger, *Phys. Rev. Lett.* **93**, 200801 (2004).
- [54] T. H. Taminiau, R. J. Moerland, F. B. Segerink, L. Kuipers, and N. F. van Hulst, *Nano Lett.* **7**, 28 (2007).
- [55] G. Behme, A. Richter, M. Süptitz, and C. Lienau, *Rev. Sci. Instrum.* **68**, 3458 (1997).
- [56] K. Karrai and R. D. Grober, *Appl. Phys. Lett.* **66**, 1842 (1995).
- [57] K. Karrai and I. Tiemann, *Phys. Rev. B* **62**, 13174 (2000).
- [58] F. J. Giessibl, *Rev. Mod. Phys.* **75**, 949 (2003).
- [59] P. Lambelet, A. Sayah, M. Pfeffer, C. Philipona, and F. Marquis-Weible, *Appl. Opt.* **37**, 7289 (1998).
- [60] V. Emiliani, F. Intonti, C. Lienau, T. Elsaesser, R. Nötzel, and K. H. Ploog, *Phys. Rev. B* **64**, 155316, (2001).
- [61] K. Brunner, G. Abstreiter, G. Böhm, G. Tränkle, and G. Weimann, *Phys. Rev. Lett.* **73**, 1138 (1994).
- [62] H. F. Hess, E. Betzig, T. D. Harris, L. N. Pfeiffer, and K. W. West, *Science* **264**, 1740 (1994).
- [63] D. Gammon, E. S. Snow, B. V. Shanabrook, D. S. Katzer, and D. Park, *Phys. Rev. Lett.* **76**, 3005 (1996).
- [64] P. Hawrylak, G. A. Narvaez, M. Bayer, and A. Forchel, *Phys. Rev. Lett.* **85**, 389 (2000).
- [65] P. Borri, W. Langbein, S. Schneider, U. Woggon, R. L. Sellin, D. Ouyang, and D. Bimberg, *Phys. Rev. Lett.* **87**, 157401 (2001).

- [66] M. Bayer and A. Forchel, *Phys. Rev. B* **65**, 041308 (2002).
- [67] T. H. Stievater, X. Li, D. G. Steel, D. Gammon, D. S. Katzer, D. Park, C. Piermarocchi, and L. J. Sham, *Phys. Rev. Lett.* **87**, 133603 (2001).
- [68] A. Zrenner, E. Beham, S. Stuffer, F. Findeis, M. Bichler, and G. Abstreiter, *Nature* **418**, 612 (2002).
- [69] L. Quiroga and N. F. Johnson, *Phys. Rev. Lett.* **83**, 2270 (1999).
- [70] A. Nazir, B. W. Lovett, S. D. Barrett, J. H. Reina, and G. A. D. Briggs, *Phys. Rev. B* **71**, 045334 (2005).
- [71] J. Danckwerts and K. J. Ahn, J. F. rstner, and A. Knorr, *Phys. Rev. B* **73**, 165318 (2006).
- [72] E. Biolatti, R. Iotti, P. Zanardi, and F. Rossi, *Phys. Rev. Lett.* **85**, 5647 (2000).
- [73] E. Biolatti, I. D'Amico, P. Zanardi, and F. Rossi, *Phys. Rev. B* **65**, 075306 (2002).
- [74] E. A. Stinaff, M. Scheibner, A. S. Bracker, I. V. Ponomarev, V. L. Korenev, M. E. Ware, M. F. Doty, T. L. Reinecke, and D. Gammon, *Science* **311**, 636 (2006).
- [75] H. Raether, *Surface Plasmons on Smooth and Rough Surfaces and on Gratings* (Springer, New York, 1988).
- [76] D. Sarid, *Phys. Rev. Lett.* **47**, 1927 (1981).
- [77] R. K. Chang and T. E. Furtak (eds.), *Surface Enhanced Raman Scattering* (Plenum Press, New York, 1982).
- [78] T. Liebermann and W. Knoll, *Colloids Surf. A* **171**, 115 (2000).
- [79] K. Okamoto, I. Niki, A. Shvartsner, Y. Narukawa, T. Mukai, and A. Scherer, *Nature Mater.* **3**, 601 (2004).
- [80] R. Köehler, A. Tredicucci, F. Beltram, H. E. Beere, E. H. Linfield, A. G. Davies, D. A. Ritchie, R. C. Iotti, and F. Rossi, *Nature* **417**, 156 (2002).
- [81] M. Vaupel, A. Eing, K. O. Greulich, J. Roegerer, P. Schellenberg, H. M. Striebel, and H. F. Arlinghaus, in: *Microarray Technology and Its Applications*, edited by D. Nicolau and U. Mueller (Springer, Berlin, Heidelberg, 2005).
- [82] M. Pokinski and H. Arwin, *Thin Solid Films* **455**, 716 (2004).
- [83] M. Righini, G. Volpe, C. Girard, D. Petrov, and R. Quidant, *Phys. Rev. Lett.* **100**, 186804 (2008).
- [84] H. J. Lezec, A. Degiron, E. Devaux, R. A. Linke, L. Martin-Moreno, F. J. Garcia-Vidal, and T. W. Ebbesen, *Science* **297**, 820 (2002).
- [85] J. D. Joannopoulos, R. D. Meade, and J. N. Winn, *Photonic Crystals: Molding the flow of light* (Princeton University Press, Singapore, 1995).
- [86] A. Dogariu, T. Thio, L. J. Wang, T. W. Ebbesen, and H. J. Lezec, *Opt. Lett.* **26**, 450 (2001).
- [87] L. Martin-Moreno, F. J. Garcia-Vidal, H. J. Lezec, K. M. Pellerin, T. Thio, J. B. Pendry, and T. W. Ebbesen, *Phys. Rev. Lett.* **86**, 1114 (2001).
- [88] Q. Cao and P. Lalanne, *Phys. Rev. Lett.* **88**, 057403 (2002).
- [89] H. F. Ghaemi, T. Thio, D. E. Grupp, T. W. Ebbesen, and H. J. Lezec, *Phys. Rev. B* **58**, 6779 (1998).
- [90] C. Genet, M. P. van Exter, and J. P. Woerdman, *Opt. Commun.* **225**, 331 (2003).
- [91] F. Reynaud, F. Salin, and A. Barthelemy, *Opt. Lett.* **14**, 275 (1989).
- [92] C. Iaconis and I. A. Walmsley, *Opt. Lett.* **23**, 792 (1998).
- [93] G. Stibenz and G. Steinmeyer, *Opt. Express* **12**, 6319 (2004).
- [94] M. Sarrazin, J.-P. Vigneron, and J.-M. Vigoureux, *Phys. Rev. B* **67**, 085415 (2003).
- [95] U. Fano, *Ann. Phys.* **424**, 393 (1938).
- [96] U. Fano, *Phys. Rev.* **124**, 1866 (1961).
- [97] A. Christ, S. G. Tikhodeev, N. A. Gippius, J. Kuhl, and H. Giessen, *Phys. Rev. Lett.* **91**, 183901 (2003).
- [98] C. Ropers, G. Stibenz, G. Steinmeyer, R. Müller, D. J. Park, K. G. Lee, J. Kim, Q. H. Park, D. S. Kim, and C. Lienau, *Appl. Phys. B* **84**, 183 (2006).
- [99] H. Lochbihler, *Phys. Rev. B* **50**, 4795 (1994).
- [100] K. G. Lee and Q. H. Park, *Phys. Rev. Lett.* **95**, 103902 (2005).
- [101] R. Hillenbrand and F. Keilmann, *Phys. Rev. Lett.* **85**, 3029 (2000).
- [102] K. V. Nerkararyan, *Phys. Lett. A* **237**, 103 (1997).
- [103] D. K. Gramotnev, D. F. P. Pile, M. W. Vogel, and X. Zhang, *Phys. Rev. B* **75**, 035431 (2007).
- [104] M. I. Stockman, *Phys. Rev. Lett.* **93**, 137404 (2004).
- [105] A. J. Babadjanyan, N. L. Margaryan, and K. V. Nerkararyan, *J. Appl. Phys.* **87**, 3785 (2000).
- [106] A. Bouhelier, J. Renger, M. R. Beversluis, and L. Novotny, *J. Microsc.* **210**, 220 (2003).
- [107] F. Keilmann, *J. Microsc.* **194**, 567 (1999).
- [108] G. Stibenz, C. Ropers, C. Lienau, C. Warmuth, A. Wyatt, I. Walmsley, and G. Steinmeyer, *Appl. Phys. B* **83**, 511 (2006).
- [109] C. C. Neacsu, G. A. Reider, and M. B. Raschke, *Phys. Rev. B* **71**, 201402 (2005).
- [110] N. Issa and R. Guckenberger, *Plasmonics* **2**, 31 (2007).
- [111] P. Hommelhoff, Y. Sortais, A. Aghajani-Talesh, and M. A. Kasevich, *Phys. Rev. Lett.* **96**, 077401 (2006).
- [112] N. Zhavoronkov, Y. Gritsai, M. Bargheer, M. Woerner, T. Elsaesser, F. Zamponi, I. Uschmann, and E. Forster, *Opt. Lett.* **30**, 1737 (2005).
- [113] V. A. Lobastov, R. Srinivasan, and A. H. Zewail, *Proc. Natl. Acad. Sci. USA* **102**, 7069 (2005).
- [114] W. E. King, G. H. Campbell, A. Frank, B. Reed, J. F. Schmerge, B. J. Siwick, B. C. Stuart, and P. M. Weber, *J. Appl. Phys.* **97**, 111101 (2005).
- [115] J. G. Fujimoto, J. M. Liu, E. P. Ippen, and N. Bloembergen, *Phys. Rev. Lett.* **53**, 1837 (1984).
- [116] W. S. Fann, R. Storz, H. W. K. Tom, and J. Bokor, *Phys. Rev. Lett.* **68**, 2834 (1992).
- [117] M. Aeschlimann, M. Bauer, and S. Pawlik, *Chem. Phys.* **205**, 127 (1996).
- [118] H. Petek and S. Ogawa, *Prog. Surf. Sci.* **56**, 239 (1997).
- [119] J. J. Quinn, *Phys. Rev.* **126**, 1453 (1962).
- [120] L. V. Keldysh, *Sov. Phys. JETP* **20**, 1307 (1965).
- [121] S. I. Anisimov, V. A. Benderskii, and G. Farkas, *Sov. Phys. Usp.* **20**, 467 (1977).
- [122] M. I. Stockman and P. Hewageegana, *Nano Lett.* **5**, 2325 (2005).
- [123] A. Kubo, K. Onda, H. Petek, Z. Sun, Y. S. Jung, and H. K. Kim, *Nano. Lett.* **5**, 1123 (2005).
- [124] R. S. Judson and H. Rabitz, *Phys. Rev. Lett.* **68**, 1500 (1992).
- [125] D. Meshulach and Y. Silberberg, *Nature* **396**, 239 (1998).
- [126] T. C. Weinacht, J. Ahn, and P. H. Bucksbaum, *Nature* **397**, 233 (1999).
- [127] T. Feurer, J. C. Vaughan, and K. A. Nelson, *Science* **299**, 374 (2003).

- [128] O. Schmidt, M. Bauer, C. Wiemann, R. Porath, M. Scharfe, O. Andreyev, G. Schonhense, and M. Aeschlimann, *Appl. Phys. B* **74**, 223 (2002).
- [129] T. Brixner, F. J. G. de Abajo, J. Schneider, and W. Pfeiffer, *Phys. Rev. Lett.* **95**, 093901 (2005).
- [130] M. Sukharev and T. Seideman, *Nano Lett.* **6**, 715 (2006).
- [131] D. J. Bergman and M. I. Stockman, *Phys. Rev. Lett.* **90**, 027402 (2003).
- [132] J. Seidel, S. Grafstroem, and L. Eng, *Phys. Rev. Lett.* **94**, 177401 (2005).
- [133] T. J. Thompson, G. Rempe, and H. J. Kimble, *Phys. Rev. Lett.* **68**, 1132 (1992).
- [134] T. Yoshie, A. Scherer, J. Hendrickson, G. Khitrova, H. M. Gibbs, G. Rupper, C. Ell, O. B. Shchekin, and D. G. Deppe, *Nature* **432**, 200 (2004).
- [135] C. Weisbuch, M. Nishioka, A. Ishikawa, and Y. Arakawa, *Phys. Rev. Lett.* **69**, 3314 (1992).
- [136] E. M. Purcell, *Phys. Rev.* **69**, 681 (1946).
- [137] J. M. Gerard, B. Sermage, B. Gayral, B. Legrand, E. Costard, and V. Thierry-Mieg, *Phys. Rev. Lett.* **81**, 1110 (1998).
- [138] K. H. Drexhage, *Prog. Opt.* **12**, 163 (1974).
- [139] I. Pockrand, A. Brillante, and D. Moebius, *J. Chem. Phys.* **77**, 6289 (1982).
- [140] N. E. Hecker, R. A. Hoepfel, and N. Sawaki, *Physica E* **2**, 98 (1998).
- [141] Y. Fedutik, V. V. Temnov, O. Schops, U. Woggon, and M. V. Artemyev, *Phys. Rev. Lett.* **99**, 136802 (2007).
- [142] W. Zhang, A. O. Govorov, and G. W. Bryant, *Phys. Rev. Lett.* **97**, 146804 (2006).
- [143] I. Gontijo, M. Boroditsky, E. Yablonovitch, S. Keller, U. K. Mishra, and S. P. DenBaars, *Phys. Rev. B* **60**, 11564 (1999).
- [144] A. Neogi, C. W. Lee, H. O. Everitt, T. Kuroda, A. Tackeuchi, and E. Yablonovitch, *Phys. Rev. B* **66**, 153305 (2002).
- [145] R. Houdre, C. Wiesbuch, R. P. Stanley, U. Oesterle, P. Pellandini, and M. Ilegems, *Phys. Rev. Lett.* **73**, 2043 (1994).
- [146] D. G. Lidzey, D. D. C. Bradley, M. S. Skolnick, T. Virgili, S. Walker, and D. M. Whittaker, *Nature* **395**, 53 (1998).
- [147] J. Dintinger, S. Klein, F. Bustos, W. L. Barnes, and T. W. Ebbesen, *Phys. Rev. B* **71**, 035424 (2005).